Bloch oscillation, dynamical localization, and optical probing of electron gases in quantum-dot superlattices in high electric fields

Danhong Huang,[1] S. K. Lyo,[2] and Godfrey Gumbs[3]
[1]*Air Force Research Laboratory, Space Vehicles Directorate, Kirtland Air Force Base, New Mexico 87117, USA*
[2]*Sandia National Laboratories, Albuquerque, New Mexico 87185, USA*
[3]*Department of Physics and Astronomy, Hunter College, City University of New York, 695 Park Avenue, New York, New York 10065, USA*

(Received 5 August 2008; revised manuscript received 8 January 2009; published 10 April 2009)

In this paper, we present numerical results for steady-state and time-dependent currents as well as for a long-time average current in strong nonlinear dc and ac electric fields for an electron gas in a one-dimensional (1D) quantum-dot superlattice. A microscopic model is employed for the scattering of electrons by phonons and static impurities by means of the Boltzmann equation method. The dc results are favorably compared with recent exact analytic results based on a relaxation-time model for electron-phonon scattering. Our results demonstrate the different roles played by elastic and inelastic scattering on the damped Bloch oscillations as well as the nonlinear steady-state current and their opposite roles on the damped dynamical localization. We also find a suppression of dynamical localization by strong Bloch oscillations and features in the Esaki-Tsu peaks in the presence of an ac electric field when electron scattering is included. On the basis of a nonequilibrium electron distribution obtained from the Boltzmann equation, a self-consistent-field approach is employed to establish a general formalism for the optical response of current-driven electrons in both the linear and nonlinear regimes to a 1D quantum-dot superlattice. The dc-field dependences of both the peak energy and peak strength in the absorption spectrum for a 1D quantum-dot superlattice are calculated, from which we find: (1) both the peak energy and its strength are significantly reduced with increasing dc electric field; and (2) the peak energy and peak strength are anomalously enhanced by raising the temperature for the nonlinear transport of electrons when a strong dc electric field is applied.

DOI: 10.1103/PhysRevB.79.155308 PACS number(s): 72.20.Ht

I. INTRODUCTION

Bloch oscillations are one of the most striking predictions from the semiclassical Boltzmann theory for electron transport. For a system consisting of independent electrons under a periodic potential, the velocity of the electron becomes a time-dependent periodic function. There have been many theoretical[1–8] and experimental[9–12] activities in this area, culminating in the observation of terahertz (THz) radiation from coherently oscillating electrons and negative differential conductance.[13] From an experimental point of view, for a very strong bias electric field in the Wannier-Stark ladder regime, optical observation of Bloch oscillations in a semiconductor superlattice was reported by Feldmann *et al.*,[14] using a transient degenerate four-wave mixing approach and by Dekorsy *et al.*,[15,16] using a time-resolved electro-optic technique. The coherent terahertz radiation originating from the Bloch oscillations was also reported by Waschke *et al.*,[17] by Bonvalet *et al.*,[18] and by Bolivar *et al.*[19] in this regime. On the contrary , from the theoretical aspect, the solution of the Boltzmann transport equation with an arbitrary one-dimensional-potential profile was reported by Dignam *et al.*,[20] using a stepwise approximation for numerical calculations with an isotropic scattering of electrons in a spherical energy band and by Meier *et al.*,[21] and Rossi *et al.*,[22] using the generalized semiconductor Bloch equations for photoexcited semiconductors with the inclusion of an electric field. The interplay between Zener tunneling and Wannier-Stark resonances was also studied by Di Carlo *et al.*,[23] using a theory based on multichannel scattering. However, to the best of our knowledge, no exact solution for the Boltzmann transport equation has been obtained so far with the full inclusion of microscopic scattering of electrons with both impurities and phonons. For a detailed discussion of Bloch oscillations in a semiconductor superlattice, readers are referred to two review articles by Wacker *et al.*[24] and by Bonilla *et al.*,[25] as well as additional references therein. In ordinary bulk semiconductors, however, Bloch oscillations cannot be seen due to the fact that collisions collectively dephase the coherent motion of electrons on a time scale which is usually much shorter than the oscillation period. The physics of semiconductor superlattices in a strong dc electric field F_{dc} is extremely rich due to the large number of parameters that can be controlled quite freely. Evidence for Bloch oscillations in doped superlattices, resulting in a negative differential conductance, predicted by Esaki and Tsu,[1] has been reported by Sibille *et al.*[9] for samples at room and low temperatures. A tunable strong THz emitter allows for real-time active spectral imaging in combination with a focal-plane detector array.[26] Under a very strong dc electric field, the Wannier-Stark ladders have to be taken into account.[27] We are interested in a moderately high nonlinear dc electric field, where the Boltzmann equation can be employed for studying the scattering effect on intraminiband transport of electrons.

Recently, one of the authors employed a relaxation-time approximation for inelastic phonon scattering and obtained an exact analytical solution of the Boltzmann equation in a one-dimensional (1D) quantum-dot superlattice,[8] shown in Fig. 1. He demonstrated differing roles played by elastic and

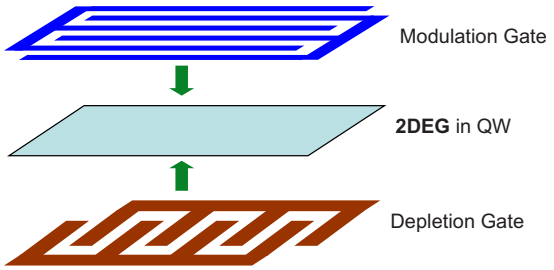

FIG. 1. (Color online) Illustration of an array of 1D quantum-dot superlattices, in which a middle two-dimensional electron-gas (2DEG) layer in a GaAs quantum well is sandwiched between a back depletion gate (with a large negative voltage), forming a quantum-wire array, and a front modulation gate (with a small negative voltage), forming periodic potential barriers along the wires.

inelastic scattering in determining the onset field for the Bloch oscillation, the field for the peak steady-state current, the peak current, and the current in the negative differential conductance region. While this analytic theory is useful in understanding the relations between the current and the scattering rates in a transparent way, it does not give a microscopic expression for the temperature dependence of the current.

If electrons in a state of equilibrium in a 1D quantum-dot superlattice are perturbed by a weak external optical field, they will respond to this probe field by forming a charge-density wave in the system. When the incident photon energy is large, interminiband transitions of electrons will occur, inducing a polarization field in the transverse direction perpendicular to the 1D quantum-dot superlattice.[28] However, if the photon energy is small, intraminiband transitions of electrons will be involved, inducing a polarization field in the longitudinal direction parallel to the axis of the 1D quantum-dot superlattice.[29,30] In the former case, the optical field can be spatially uniform, while in the latter case, the required optical field must be spatially nonuniform. The dynamics of perturbed electrons in the 1D quantum-dot superlattice can be accounted for by the self-consistent theory in the linear-response regime.[28–30] Even after the electrons in a 1D quantum-dot superlattice have been driven into a nonequilibrium state, we can still perturb these nonequilibrium electrons using a weak optical field. In this case, we expect that both the peak energy (including the single-particle transition energy as well as the many-body depolarization shift) and the peak strength in the absorption spectrum can be easily controlled by a dc electric field. To the best of our knowledge, a general theory for the optical response of driven electrons under a strong bias is currently still not available.[31]

In this paper, we present a rigorous numerical solution for the transient and steady-state currents in the presence of dc and ac fields for an electron gas in the same system with the inclusion of the effects of elastic and inelastic scattering by treating electron-phonon scattering *microscopically*. In a dc field without an ac component, our result demonstrates quantitatively how scattering damps the Bloch oscillations and affects the peak field, peak current, and high-field current for a degenerate as well as nondegenerate electronic system. For this purpose, we study the response of the current when we vary the strengths of electron-phonon scattering and impurity scattering by using separate scaling parameters. The results from these scaling studies are consistent with the predictions of the analytic model of Lyo.[8]

Recent research and development of high-power tunable THz radiation sources have spurred strong interest in the dynamics of electrons in ac electric fields beyond microwave frequencies. When electrons are subject to a combination of strong dc and ac electric fields

$$F(t) = F_{\rm dc} + F_{\rm ac}\cos(2\pi\nu_{\rm ac}t), \tag{1}$$

where $F_{\rm ac}$ and $\nu_{\rm ac}$ represent the ac-field amplitude and frequency, a number of resonant structures are predicted theoretically in the I-V characteristic curve.[32–35] Within the nearest-neighbor tight-binding approximation, each of these resonant structures possesses a line shape similar to the Esaki-Tsu peak[36] but is shifted by an amount of $n(h\nu_{\rm ac}/ed)$, where $n=1,2,\cdots$ and d is the superlattice period. Studies on the long-time average current under ac monochromatic[37] and bichromatic[36] electric fields have been reported recently, in which the conditions for the so-called dynamical localization[38–40] were derived either for a scattering-free system or within the relaxation-time approximation for elastic scattering. Conditions for dynamical localization in generalized ac electric fields have also been obtained, when a band structure beyond the nearest-neighbor approximation was employed.[40,41]

For an ac electric field superimposed on a dc field, we present a rigorous numerical solution for the transient current and the long-time-average current in a 1D miniband. Our numerical result demonstrates how elastic scattering suppresses the dynamical localization and the associated higher harmonics and, at the same time, how inelastic scattering enhances the dynamical localization. The results allow us to display quantitatively the opposite roles played by elastic and inelastic scattering on the dependences of the current on $F_{\rm ac}$ and $\nu_{\rm ac}$. In the current work, only one shifted Esaki-Tsu peak with $n=1$ is found after the damping is included.

When the current-driven nonequilibrium electrons in a 1D quantum-dot superlattice are subject to a spatially nonuniform x-polarized optical probe field

$$\mathrm{E}_{\rm op}(x;t) = \exp(i\tilde{\omega}t - iqx)\mathcal{E}_{\rm op}(q), \tag{2}$$

where q is the wave number of the probe field, $\tilde{\omega}=\omega-qv_d \geq 0$ to include the Doppler effect, v_d is the drift velocity of driven electrons [see its definition after Eq. (34)], and $\hbar\omega$ is the energy of the probing photons, a self-consistent-field theory is employed to calculate the linear optical-absorption spectrum, including the dc-field dependence of the peak energy and peak strength when $F_{\rm ac}=0$. From our studies, we find that both the peak energy and its strength are significantly reduced with increasing dc electric field. Additionally, we find that both the peak energy and the peak strength are reduced, as expected, whenever the temperature is increased in the low-field regime for the linear transport of electrons in a 1D quantum-dot superlattice. However, an unexpected different behavior is obtained for the increased peak energy and enhanced peak strength by raising the temperature in the high-field regime for the nonlinear transport of electrons.

The paper is organized as follows. In Sec. II, we introduce our model and theory based on the Boltzmann equation for both the Bloch oscillations and dynamical localization, along with a procedure for accurate numerical calculations. In the same section, we further introduce a self-consistent-field approach for calculating optical absorption by current-driven nonequilibrium electrons in a 1D quantum-dot superlattice. In Sec. III, numerical results are presented for both the Bloch oscillations and dynamical localization. In addition, we also present the numerical results in Sec. III for the dc-field dependence of peak energy and peak strength in the absorption spectrum. The paper is briefly concluded in Sec. IV.

II. MODEL AND THEORY

In this section, we discuss a microscopic form of the Boltzmann equation in a 1D quantum-dot superlattice. Scattering by impurities and acoustic phonons is included. We assume a strong quadratic potential for the transverse confinement and a tight-binding model for electron tunneling in the superlattice direction. A rigorous numerical approach is discussed for the solution of the time-dependent nonequilibrium distribution function and the nonlinear current in the strong-field regime.

A. Boltzmann equation

Let us start by considering a degenerate electron gas moving in a 1D quantum-dot superlattice with a period d in the superlattice (x)-direction. For this system with a strong transverse confining potential, only the lowest subband will be occupied by electrons in the low-density and low-temperature regimes, and therefore, a single subband model will be adequate. Moreover, the so-called Umklapp scattering process can be neglected due to the existence of a large miniband gap and small phonon energies allowed at low temperatures. Simultaneously, both the magnitude of dc field and the amplitude of ac field are limited to a degree that the field-induced potential drop between any two adjacent superlattice unit cells cannot exceed the width of the miniband. The original form of the Boltzmann transport equation for a time-dependent distribution function $f(k,t)$ of electrons is given by[42,43]

$$\frac{\partial f(k,t)}{\partial t} = \frac{eF(t)}{\hbar}\frac{\partial f(k,t)}{\partial k} + \sum_{k'} P_e(k,k')[f(k',t) - f(k,t)] + \sum_{k',\mathbf{q},\lambda} \big(P_+(k,k')\{(n_{q\lambda}+1)f(k',t)[1-f(k,t)] - n_{q\lambda}f(k,t)[1-f(k',t)]\} + P_-(k,k')\{n_{q\lambda}f(k',t)\times[1-f(k,t)] - (n_{q\lambda}+1)f(k,t)[1-f(k',t)]\}\big), \tag{3}$$

where $F(t)$ represents the applied (time-dependent) electric field defined in Eq. (1), k is the electron wave vector along the x direction, $\mathbf{q}$ is the three-dimensional (3D) wave vector of phonons, $\lambda=\ell$ ($\lambda=t$) corresponds to the longitudinal (transverse) acoustic phonons, and $n_{q\lambda}=N_0(\omega_{q\lambda})$ is the Bose function for the equilibrium phonons with the frequency $\omega_{q\lambda}$ in the mode of $\mathbf{q}$ and λ. In Eq. (3), we have defined the electron-phonon inelastic-scattering transition probability rate as[42,43]

$$P_{\pm}(k,k') = \frac{2\pi}{\hbar}|V_{k,k'}|^2\delta(\varepsilon_k - \varepsilon_{k'} \pm \hbar\omega_{q\lambda})\delta_{k',k\pm q_x}, \tag{4}$$

and the electron-impurity elastic-scattering transition probability rate as[44]

$$P_e(k,k') = \frac{2\pi}{\hbar}|U_{k,k'}|^2\delta(\varepsilon_k - \varepsilon_{k'}), \tag{5}$$

where $\varepsilon_k = W[1-\cos(kd)]/2$ is the electron kinetic energy with a bandwidth W in the single-band tight-binding model, $V_{k,k'}$ represents the interaction between electrons and phonons, and $U_{k,k'}$ is the interaction between electrons and impurities.

We define $f(k,t)=f_k^{(0)}+g_k(t)$ with a dynamical nonequilibrium part $g_k(t)$ for the total distribution function, where $f_k^{(0)}=f_0(\varepsilon_k)$ is the Fermi function for the equilibrium electrons. We then note that the terms of zeroth order in g_k in the scattering parts of Eq. (3) cancel out due to detailed balance. After incorporating these considerations, we can algebraically simplify Eq. (3) into

$$\frac{\partial g_k(t)}{\partial t} = -eF(t)v_k\left[-\frac{\partial f_k^{(0)}}{\partial \varepsilon_k}\right] + \frac{eF(t)}{\hbar}\frac{\partial g_k(t)}{\partial k} + [g_{-k}(t) - g_k(t)]\sum_{k'\in -k} P_e(k,k') - g_k(t)\sum_{k',\mathbf{q},\lambda} \times\{P_+(k,k')(n_{q\lambda}+f_{k'}^{(0)}) + P_-(k,k')(n_{q\lambda}+1-f_{k'}^{(0)}) + g_{k'}(t)[P_+(k,k') - P_-(k,k')]\} + \sum_{k',\mathbf{q},\lambda} g_{k'}(t)[P_+(k,k') \times(n_{q\lambda}+1-f_k^{(0)}) + P_-(k,k')(n_{q\lambda}+f_k^{(0)})], \tag{6}$$

where $v_k=(1/\hbar)d\varepsilon_k/dk$ is the group velocity of electrons with the wave vector k and the k' sum for $k'\in -k$ is carried out near the resonance at $k'=-k$.

B. Elastic and inelastic-scattering rates

The transport relaxation rate from electron-impurity scattering equals[44]

$$\frac{1}{\tau_k} \equiv 2\sum_{k'\in -k} P_e(k,k') = \frac{\pi}{\hbar}|U_{k,-k}|^2\mathcal{D}(\varepsilon_k). \tag{7}$$

Here, the factor 2 arises from the $2k_F$ (k_F is the Fermi wave vector at zero temperature) scattering across the Fermi sea and $\mathcal{D}(\varepsilon)$ is the total density of states given by

$$\mathcal{D}(\varepsilon) = \frac{2L_x}{\pi d}\frac{1}{\sqrt{(W-\varepsilon)\varepsilon}}, \tag{8}$$

where L_x is the length of the superlattice.

For electron-phonon scattering, we define scattering rates

$$W_{\pm}(k,k') \equiv \sum_{\mathbf{q},\lambda} P_{\pm}(k,k'). \tag{9}$$

Using Eq. (4) and writing $\hbar\omega_{q\lambda}=\alpha_\lambda\sqrt{(k-k')^2+q_\perp^2}$ from the Debye model, we find[42,43]

$$W_{\pm}(k,k') = \frac{\mathcal{S}}{\hbar}\sum_{\lambda} \theta[(\varepsilon_k-\varepsilon_{k'})^2-\alpha_\lambda^2(k-k')^2] \times \theta(\pm\varepsilon_{k'}\mp\varepsilon_k)\hbar\frac{\hbar\omega_{q\lambda}|V_\lambda(\mathbf{q})|^2}{\alpha_\lambda^2}\Phi(q_\perp), \tag{10}$$

where $\theta(x)$ is the unit step function, $\mathcal{S}$ is the samples cross-sectional area, $\alpha_\lambda=\hbar c_\lambda$, c_λ is the velocity of sound for the phonon of λ mode, $q_x=|k'-k|$,

$$q_\perp = \sqrt{q_y^2+q_z^2} = \frac{1}{\alpha_\lambda}\sqrt{(\varepsilon_k-\varepsilon_{k'})^2-\alpha_\lambda^2(k-k')^2}, \tag{11}$$

$$q = \sqrt{q_x^2+q_\perp^2} = \frac{|\varepsilon_k-\varepsilon_{k'}|}{\alpha_\lambda}, \tag{12}$$

and the form factor in Eq. (10) takes the form

$$\Phi(q_\perp) = \exp(-q_\perp^2R^2/2) = \exp\{-[(\varepsilon_k-\varepsilon_{k'})^2-\alpha_\lambda^2(k-k')^2]R^2/2\alpha_\lambda^2\} \tag{13}$$

for a transverse parabolic confinement within the yz plane with the radius R for the cylindrical confinement model. The quantity $\Phi(q_\perp)$ arises from the consequence of momentum conservation for $q_\perp$. A smaller value of R in Eq. (13) implies stronger electron-phonon scattering in Eq. (10).

Upon assuming axial symmetry, we find that the strength of the electron-phonon interaction $|V_\lambda(\mathbf{q})|^2$ in Eq. (10) is given by[42]

$$\hbar\omega_{q\lambda}|V_\lambda(\mathbf{q})|^2 = \frac{(\hbar\omega_{q\lambda})^2}{2\epsilon_{\mathrm{TF}}(q_x)^2\rho_Mc_\lambda^2\mathcal{V}}\left[D^2\delta_{\lambda,\ell}+\left(\frac{eh_{14}}{q}\right)^2A_{\mathbf{q}\lambda}\right], \tag{14}$$

where $\mathcal{V}=\mathcal{S}L_x$ is the sample volume, ρ_M is the mass density, D is the deformation-potential coefficient, h_{14} is the piezoelectric constant, $\epsilon_{\mathrm{TF}}(q_x)$ is the Thomas-Fermi dielectric function,[42] and $A_{\mathbf{q}\lambda}$ is the structure factor for acoustic phonons[42] due to anisotropic electron-phonon coupling. We further note from Eq. (10) that only one of $W_\pm(k,k')$ is nonzero, i.e., either $W_+(k,k')>0$ for $\varepsilon_{k'}>\varepsilon_k$ or $W_-(k,k')>0$ for $\varepsilon_{k'}<\varepsilon_k$. This directly yields the result

$$W_{\pm}(k,k') = \theta(\pm\varepsilon_{k'}\mp\varepsilon_k)\sum_\lambda W_\lambda(k,k'), \tag{15}$$

where $W_\lambda(k,k')=W_\lambda(k',k)$ is given by

$$W_\lambda(k,k') = \frac{\mathcal{S}}{\hbar}\theta[(\varepsilon_k-\varepsilon_{k'})^2-\alpha_\lambda^2(k-k')^2]|V_\lambda(\mathbf{q})|^2\frac{q}{\alpha_\lambda}\Phi(q_\perp). \tag{16}$$

C. Numerical procedure

Using the scattering rates introduced in Secs. II A and II B, we may rewrite Eq. (6) into the concise form

$$\frac{\partial g_k(t)}{\partial t} = eF(t)v_k\frac{\partial f_k^{(0)}}{\partial\varepsilon_k}+\frac{eF(t)}{\hbar}\frac{\partial g_k(t)}{\partial k} + \frac{1}{2\tau_k}[g_{-k}(t)-g_k(t)] - g_k(t)\sum_{k'}\{W_+(k,k')(n_{k,k'}+f_{k'}^{(0)}) + W_-(k,k')(n_{k,k'}+1-f_{k'}^{(0)}) + g_{k'}(t) \times[W_+(k,k')-W_-(k,k')]\} + \sum_{k'} g_{k'}(t) \times[W_+(k,k')(n_{k,k'}+1-f_k^{(0)}) + W_-(k,k')(n_{k,k'}+f_k^{(0)})], \tag{17}$$

where $n_{k,k'}=N_0(|\varepsilon_k-\varepsilon_{k'}|/\hbar)$ is independent of $\lambda=\ell,t$. By introducing the notations $f_k^-=f_k^{(0)}$ and $f_k^+=1-f_k^{(0)}$, we obtain the discrete form for the total inelastic-scattering rate

$$W_j = \frac{L_x}{2\pi}\delta k\sum_{j',\pm} W_\pm(k,k')(n_{k,k'}+f_{k'}^{\mp}), \tag{18}$$

where $k\equiv j\delta k$ and $k'\equiv j'\delta k$ for $1\le j\le N$, $\delta k=2\pi/(N-1)d$ with $N\gg1$ being an odd integer, and

$$W_{j,j'} = \sum_{\pm} W_\pm(k,k')(n_{k,k'}+f_{k'}^{\pm}). \tag{19}$$

We can also write

$$W_j^g(t) = \frac{L_x}{2\pi}\delta k\sum_{j'} g_{k'}(t)[W_+(k,k')-W_-(k,k')], \tag{20}$$

and

$$\frac{dg_k(t)}{dt} = eF(t)v_k\frac{\partial f_k^{(0)}}{\partial\varepsilon_k}+\frac{eF(t)}{\hbar}\frac{\partial g_k(t)}{\partial k}-g_k(t)[W_j+W_j^g(t)] + \frac{1}{2\tau_k}[g_{-k}(t)-g_k(t)]+\frac{L_x}{2\pi}\delta k\sum_{j'} g_{k'}(t)W_{j,j'}. \tag{21}$$

In Eq. (21), the quantity $g_kW_j^g$ is the only nonlinear term in g_k.

Equation (21) is equivalent to the following matrix equation for $1\le j\le N$:

$$\frac{dg_j(t)}{dt} = b_j(t)-\sum_{j'=1}^{N} a_{j,j'}(t)g_{j'}(t), \tag{22}$$

where $k\equiv j\delta k$ and $k'\equiv j'\delta k$. The elements for the vector $\mathbf{b}(t)$ in Eq. (22) are

$$b_j(t) = eF(t)v_j\frac{\partial f_j^{(0)}}{\partial\varepsilon_j}, \tag{23}$$

and the elements for the matrix $\vec{\mathbf{a}}(t)$ in Eq. (22) are

$$a_{j,j'}(t) = \delta_{j,j'}\left[W_j + W_j^g(t) + \frac{1-\delta_{j,(N+1)/2}}{2\tau_j} \right] - \delta_{j+j',N+1}\left[\frac{1-\delta_{j,(N+1)/2}}{2\tau_j} \right] - \frac{eF(t)}{\hbar\delta k} c_{j,j'} - \frac{L_x}{2\pi}\delta k W_{j,j'}. \quad (24)$$

By assuming that the field $F(t)$ is turned on at $t=0$, the differential Eq. (22) can be solved in combination with the initial condition $g_j(0)=0$ for $j=1,2,\ldots,N$. In addition, using the so-called three-point central-difference formula,[45] which transforms the partial differential term $[eF(t)/\hbar]\partial g_k(t)/\partial k$ in Eq. (21) into a finite-difference term, we can write $c_{j,j'}$ in Eq. (24) in a simple form

$$c_{j,j'} = \frac{1}{2}(\delta_{j,j'-1} - \delta_{j,j'+1}). \quad (25)$$

Unfortunately, the quantities $\{g_1, g_2, \ldots, g_N\}$ are not linearly independent of each other,[43,44,46] which implies that the matrix $\vec{\vec{\mathbf{a}}}(t)$ in Eq. (22) is a singular one. In fact, the condition for the particle-number conservation requires that

$$\sum_{j=1}^{N} g_j(t) = 0. \quad (26)$$

Combined with the fact that $\varepsilon_k=\varepsilon_{-k}$ and $v_k=-v_{-k}$, this yields for $1\le j\le N$

$$g_1(t) = g_N(t) = -\frac{1}{2}\sum_{j=2}^{N-1} g_j(t), \quad (27)$$

where $j=1$ and N are the two k-space points at the first Brillouin-zone boundary. As a result of Eq. (27), we can renormalize the singular $(N\times N)$-matrix $\vec{\vec{\mathbf{a}}}(t)$ in Eq. (22) into a regular $[(N-1)\times(N-1)]$-matrix $\vec{\vec{\mathbf{a}}}'(t)$ through the following relation:

$$a'_{j,j'}(t) = a_{j,j'}(t) - \langle a_j(t)\rangle, \quad (28)$$

where $\langle a_j(t)\rangle=[a_{j,1}(t)+a_{j,N}(t)]/2$ and $j,j'=2,3,\ldots,N-1$. Consequently, Eq. (22) is renormalized and becomes

$$\frac{dg'_j(t)}{dt} = b'_j(t) - \sum_{j'=2}^{N-1} a'_{j,j'}(t) g'_{j'}(t), \quad (29)$$

where the vectors $\mathbf{g}'(t)$ and $\mathbf{b}'(t)$ are the same as the vectors $\mathbf{g}(t)$ and $\mathbf{b}(t)$, respectively, without the first and last elements with $j=1$ and N. Similarly way, we correspondingly rewrite Eq. (20), by excluding the elements with $j=1$ and N, as

$$W_j^g(t) = \frac{L_x}{2\pi}\delta k \sum_{j'=2}^{N-1} g'_{j'}(t)[W_+(j,j') - W_-(j,j') - (\langle W_+(j)\rangle - \langle W_-(j)\rangle)], \quad (30)$$

where $\langle W_\pm(j)\rangle=[W_\pm(j,1)+W_\pm(j,N)]/2$.

The time-dependent current of the system can be found from

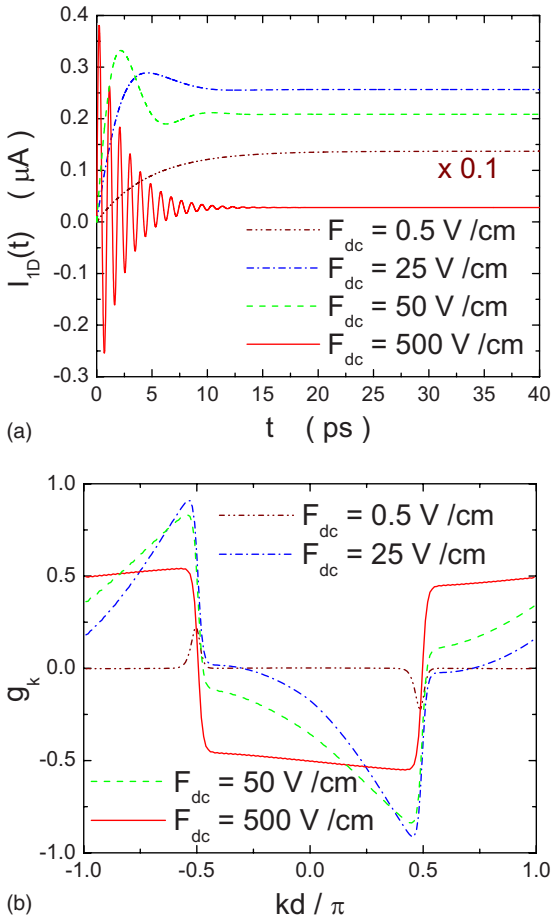

FIG. 2. (Color online) Calculated transient currents $I_{1D}(t)$ as a function of time t [in (a)] and the k dependence of the steady-state nonequilibrium part g_k of the total distribution function [in (b)] for four different values of the dc electric field, i.e., F_{dc}=0.5 (brown dashed-double-dotted curves), 25 (blue dashed-dotted curves), 50 (green dashed curves), and 500 V/cm (red solid curves). Here, we take $F_{ac}=0$, $n_{1D}=1\times10^5$ cm^{-1}, $\gamma_0=3.75\times10^{10}$ s^{-1}, $d=100$ nm, $W=5$ meV, $T=1$ K, and $R=10$ Å. The label ×0.1 in (a) indicates that the scale of the brown dashed-double-dotted curve has been multiplied by a factor of 10.

$$I_{1D}(t) = -\frac{eWd\delta k}{2\pi\hbar}\sum_{j=2}^{N-1} g'_j(t)\sin\left[\left(j-\frac{N+1}{2}\right)\delta k d\right], \quad (31)$$

and the steady-state current I_0 for a dc electric field is given by $I_{1D}(t)$ at the $t\to\infty$ limit. In the presence of an ac electric field, the ac current $I_{1D}(t)$ quickly establishes regular periodic oscillations after the scattering time. We can therefore define a long-time average current $\langle I_{1D}\rangle$ from the transient current $I_{1D}(t)$ through its limiting behavior[36]

$$\langle I_{1D}\rangle = \lim_{t_0\to\infty}\frac{1}{t_0}\int_0^{t_0} I_{1D}(t)dt, \quad (32)$$

where t_0 is much larger than the scattering time. The latter is about 10–20 picoseconds for our chosen parameters according to Figs. 2, 3, and 7. The long-time-averaged quantity $\langle I_{1D}\rangle$ includes contributions from both the dc and ac electric

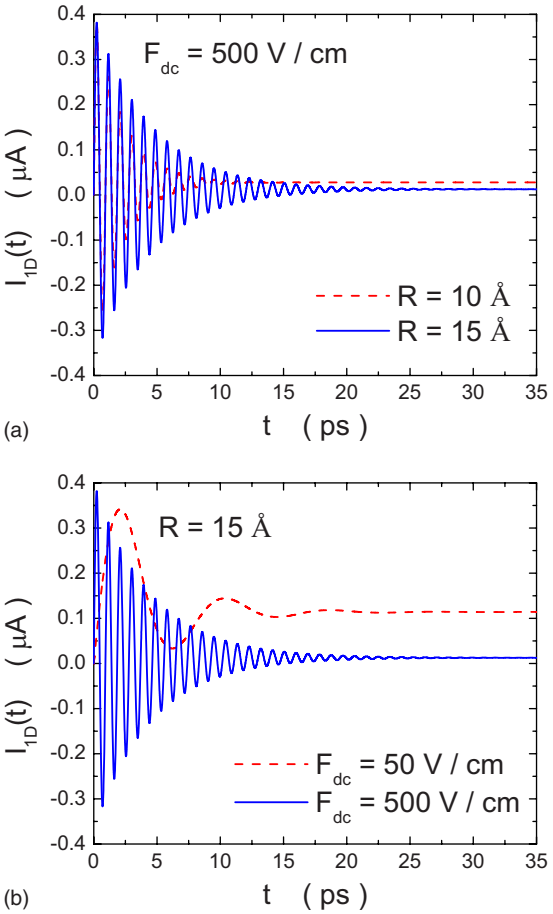

FIG. 3. (Color online) Calculated transient currents $I_{1D}(t)$ at $F_{dc}=500$ V/cm [in (a)] for two values of the radius, i.e., $R=10$ Å (red dashed curve) and $R=15$ Å (blue solid curve), and for two values of the dc electric field with $R=15$ Å [in (b)], i.e., $F_{dc}=50$ V/cm (red dashed curve) and $F_{dc}=500$ V/cm (blue solid curve). The other parameters are taken as the same as those in Fig. 2.

fields. Mathematically, $\langle I_{1D}\rangle$ represents the time-independent term after the Fourier transform $I_{1D}(t)$ is taken with respect to t .

The first-order nonlinear integro-differential transport equation in Eq. (29) is solved numerically by using an iteration scheme on the uniform discrete time points $t_n=n\delta t(n=0,1,2,\ldots)$ with a sufficiently small time step δt. Initially, we find $g'_j(t_1)$ by multiplying the expression on the right-hand side of Eq. (29) with δt and using $g'_{j'}(t_0)=0$. Here, all the site indices run from$j,j'=2,\ldots,N-1$ excluding the two end points. The electric fields are turned on at $t=0$. This process is repeated by equating $g'_j(t_n)-g'_j(t_{n-1})$ to the δt times the expression on the right-hand side of Eq. (29) in terms of $g'_{j'}(t_{n-1})$. The quantity δt is taken as being sufficiently small to ensure a convergence for the final result $g'_{j'}(t)$.

D. Current-driven optical response

When a weak electromagnetic field impinges on a condensed-matter system, the induced optical coherence will be represented by the finite off-diagonal matrix elements of a density matrix. However, in this case, the diagonal matrix elements of this density matrix still describe the *equilibrium* distribution of electrons within the resulting perturbed picture. We also note that the states of a dynamical system driven solely by a dc electric field F_{dc} (with $F_{ac}=0$) will be designated as a *nonequilibrium* distribution function although the off-diagonal matrix elements of a density matrix are still zero in the absence an optical field. Therefore, a system which is under the influence of both a weak electromagnetic field and a strong dc bias can be chosen to exhibit the optical response of current-driven nonequilibrium electrons.

In a linear-response theory for a weak optical field, the induced density in a 1D quantum-dot superlattice takes the form fluctuations in the density[28]

$$\delta n(x,\vec{\rho};\omega)=\delta n(x;\omega)\left[\frac{\alpha^2(\rho)}{2\pi}\right], \tag{33}$$

where

$$\delta n(x;\omega)=2\sum_{k,k'}\Pi^{(0)}_{k,k'}(\tilde{\omega})\mathcal{H}'_{k,k'} \times\left[\frac{1}{N_c}\sum_{j,j'}e^{ikjd-ik'j'd}\phi^*(x-j'd)\phi(x-jd)\right]. \tag{34}$$

And wherein $\Pi_0^{k,k'}(\omega)$In Eqs. (33) and (34), $\alpha(\rho)$ and $\phi(x)$ are the ground-state wave functions of electrons in the radial and x-directions, respectively (see Appendix A). The drift velocity v_d of electrons in the 1D quantum-dot superlattice is simply given by $v_d=I_0/(en_{1D})$, where n_{1D} is the linear density of electrons and I_0 is the steady-state current given by Eq. (31) in the limit of $t\to\infty$ under a dc electric field F_{dc}. The spatially nonuniform probe field can be introduced by using a surface metal grating along the x-direction. In Eq. (34), we have defined $\Pi^{(0)}_{k,k'}(\tilde{\omega})=[f(k,t)-f(k',t)]/[\hbar\tilde{\omega}-(\varepsilon_{k'}-\varepsilon_k)]$. In addition, $\mathcal{H}'_{k,k'}$ in Eq. (34) represents the matrix element of a perturbed Hamiltonian, which is calculated as [see Appendix A for the definition of the form factor $\mathcal{F}(q)$]

$$\mathcal{H}'_{k,k'}=ie\mathcal{E}_{op}(q')\left[\frac{\mathcal{F}^*(q')}{q'}\right]\delta_{k',k+q'+l'G}, \tag{35}$$

where l' is an arbitrary integer, and only the on-site overlap of wave functions is included.[28] Also, $G=2\pi/d$ in Eq. (35) is the smallest reciprocal-lattice vector.

When a probe field is applied, the induced optical polarization in the system can be calculated as[47] [see Appendix B for the derivation of $\mathcal{P}(q)$]

$$\mathcal{P}(q)=\frac{-e^2}{\mathcal{S}d}\chi^{(0)}(q;\omega-qv_d)\left[\frac{\mathcal{F}(q)}{q}\right]\sum_{l'}\left[\frac{\mathcal{F}^*(q+l'G)}{(q+l'G)}\right] \times\mathcal{E}_{op}(q+l'G). \tag{36}$$

Here, $\mathcal{S}=\pi R^2$ is the cross-sectional area of the sample and $\chi^{(0)}(q;\tilde{\omega})\equiv\chi^{(0)}(q;\omega-qv_d)$ is the Doppler-shifted irreducible polarization.

The total probe-field-induced polarization energy of the system is calculated from

$$\sum_l \mathcal{P}(q+lG)\mathcal{E}_{\rm op}^*(q+lG) = \frac{-e^2}{\mathcal{S}d}\chi^{(0)}(q;\omega-qv_d) \times \left|\sum_l \left[\frac{\mathcal{F}(q+lG)}{(q+lG)}\right] \times \mathcal{E}_{\rm op}^*(q+lG)\right|^2. \quad (37)$$

By assuming that $\mathcal{E}_{\rm op}(q)\equiv\mathcal{E}_0$, we can calculate the dimensionless Lorentz ratio[47] from the total probe-field-induced polarization energy in Eq. (37) divided by $\epsilon_0|\mathcal{E}_0|^2$, which is given by

$$\alpha_L(q;\omega) = \frac{-e^2}{\epsilon_0\mathcal{S}d}\chi^{(0)}(q;\omega-qv_d)\left|\sum_l \frac{\mathcal{F}(q+lG)}{(q+lG)}\right|^2. \quad (38)$$

The optical response of the system can be derived from the Lorentz ratio. As a matter of fact, the loss function $\mathrm{Im}[\alpha_L(q;\omega)]$ is directly associated with the optical absorption by electrons in the 1D quantum-dot superlattice, while $\mathrm{Re}[\alpha_L(q;\omega)]$ gives rise to the modulation of refractive index of the system by electrons.

The many-body effects can be described by introducing a dielectric function $\epsilon(q;\omega)$ of electrons in the 1D quantum-dot superlattice, which replaces a bare irreducible polarization function $\chi^{(0)}(q;\omega-qv_d)$ introduced in Eq. (38) by a screened one $[\chi^{(0)}(q;\omega-qv_d)/\epsilon(q;\omega)]$. In the calculation of $\epsilon(q;\omega)$, we adopt the self-consistent-field approach,[48,49] which is given by [see Appendix C for the derivation of $\epsilon(q;\omega)$ and the definition of $V_c(|q|)$]

$$\epsilon(q;\omega) = 1-\chi^{(0)}(q;\omega-qv_d)\sum_l V_c(|q+lG|)|\mathcal{F}(q+lG)|^2. \quad (39)$$

By using the derived dielectric function in Eq. (39), the Coulomb-renormalized loss function $\mathrm{Im}[\alpha_L(q;\omega)]$ is found to be

$$\mathrm{Im}[\alpha_L(q;\omega)] = \frac{e^2}{\epsilon_0\mathcal{S}d}\mathcal{A}[F_{\rm dc}] \times \left|\sum_l \frac{\mathcal{F}(q+lG)}{(q+lG)}\right|^2\left[\frac{W\sin^2(qd/2)}{\mathcal{D}(q)}\right] \times \delta[\hbar\omega-\hbar qv_d-\mathcal{D}(q)], \quad (40)$$

where (see Appendix C)

$$\mathcal{A}[F_{\rm dc}] = d\int_{-\pi/d}^{\pi/d} dk f(k,t)\cos(kd) \quad (41)$$

is the $F_{\rm dc}$-dependent amplitude factor which is related to the inverted center of mass in the quantum-dot superlattice direction,[50] and

$$\mathcal{D}(q) = \left\{\mathcal{A}[F_{\rm dc}]\frac{2W\sin^2(qd/2)}{\pi}\sum_l V_c(|q+lG|) \times |\mathcal{F}(q+lG)|^2\right\}^{1/2} \quad (42)$$

is the depolarization shift $\mathcal{D}(q)$.

The current-driven effect on the optical response of electrons in a 1D quantum-dot superlattice is reflected in the v_d dependence of the loss function $\mathrm{Im}[\alpha_L(q;\omega)]$ in Eq. (40).

III. NUMERICAL RESULTS AND DISCUSSIONS

For ease of notation, we define $\tau_j=\tau_k$ at the energy $\varepsilon_j=\varepsilon_k$ in Eq. (7),

$$\frac{1}{\tau_j} = \gamma_0\sqrt{\frac{(W-\mu)\mu}{(W-\varepsilon_j)\varepsilon_j}}, \quad (43)$$

where γ_0 is the value of $1/\tau_j$ at $\varepsilon_j=\mu$. For a fixed electron temperature T and linear density $n_{\rm 1D}$, the electron chemical potential μ is determined from the following relation:

$$n_{\rm 1D} = \frac{\delta k}{\pi}\sum_{j=1}^{N}\frac{1}{\exp[(\varepsilon_j-\mu)/k_BT]+1}. \quad (44)$$

The Fermi wave vector equals $k_F=\pi n_{\rm 1D}/2$ at $T=0$ K. We choose GaAs as the host material for our numerical calculations and employ the following parameters:[51] the velocities of sound $c_\ell=5.14\times10^5$ cm/sec, $c_t=3.04\times10^5$ cm/sec, the mass density $\rho_M=5.3$ g/cm^3, the piezoelectric constant $h_{14}=1.2\times10^7$ V/cm, the deformation-potential coefficient $D=-9.3$ eV, the host-material dielectric constant $\epsilon_b=12$, and the half width $\lambda=d/4$. For the Bloch oscillations, we consider a dc field. For dynamical localization, on the other hand, a combination of dc and ac fields is considered. The other parameters will be directly indicated in the figure captions.

A. Damped Bloch oscillations

Figure 2(a) displays the time-dependent current $I_{\rm 1D}(t)$ for various strengths of applied dc fields $F_{\rm dc}$. For $F_{\rm dc}=0.5$ V/cm (brown dashed-double-dotted curve), a transient current reaches the steady-state value very quickly without experiencing any Bloch oscillations. This indicates that the Bloch oscillations of the system are completely suppressed by electron scattering. When the dc field is increased to $F_{\rm dc}=25$ V/cm (blue dashed-dotted curve), the Bloch oscillations are barely seen with only one current maximum around $t=5$ ps after the field is turned on. Here, the Bloch oscillations are overly damped. When $F_{\rm dc}$ is further increased to 50 V/cm (green dashed curve), the Bloch oscillations start to become visible with one complete oscillation. In this case, the Bloch oscillations are heavily damped. Finally, for $F_{\rm dc}=500$ V/cm (red solid curve) the Bloch oscillations are significant with many periods of oscillation, where the Bloch oscillations are only slightly damped. This high field is employed to bring out the effect, although the Boltzmann model may not apply in the strict sense because the potential-energy

drop across the period equals the bandwidth. We show in Fig. 2(b) the steady-state nonequilibrium part g_k of the distribution function as a function of the wave vector k along the superlattice direction. For $F_{dc}=0.5$ V/cm (brown dashed-double-dotted curve), we find a positive (negative) peak in g_k around $k=-k_F$ ($k=k_F$). Here, the two Fermi edges sit at $\pm k_F d \approx \pm \pi/2$, respectively, in a 1D quantum-dot superlattice for our chosen density. The slight asymmetry in positive and negative peaks gives rise to a net steady-state current. As the dc field is increased to $F_{dc}=25$ V/cm (blue dashed-dotted curve), the positive peak at $k=-k_F$ becomes stronger and expands leftward to the Brillouin-zone boundary at $k=-\pi/d$. Simultaneously, the negative peak at $k=k_F$ also enhances itself and pushes toward $k=-k_F$. In addition, g_k starts to build up itself at the other Brillouin-zone boundary ($k=\pi/d$) to meet the k-space periodicity requirement. As the dc field further increases to $F_{dc}=50$ V/cm (green dashed curve), these observed features in g_k at $F_{dc}=25$ V/cm are further enlarged until a constant $g_k \approx \pm 0.5$ is reached separately within three successive regions, i.e., $-\pi/d \le k < -k_F$, $-k_F \le k < k_F$, and $k_F \le k < \pi/d$ for $F_{dc}=500$ V/cm (red solid curve). This high-field behavior in g_k implies that the total steady-state distribution function will show up nearly as a constant of 0.5 across the whole Brillouin zone, in strong contrast with the square shape of the initial distribution function of equilibrium electrons at low temperatures.

Figure 3(a) presents transient currents $I_{1D}(t)$ for two values of the localization radius R at a high dc field $F_{dc}=500$ V/cm. For $R=15$ Å (blue solid curve), the large-amplitude Bloch oscillations are found with a very small steady-state current before the decoherence time $T_2 \approx 15$ ps (beyond which the Bloch oscillations decay) is reached. On the other hand, the amplitude of the initial Bloch oscillations is significantly reduced for $R=10$ Å (red dashed curve), where phonon scattering is relatively stronger. However, the steady-state current in this case is enhanced. We display in Fig. 3(b) the transient currents $I_{1D}(t)$ for two values of F_{dc} with the same localization radius $R=15$ Å. In comparison with the complete Bloch oscillations at a high field $F_{dc}=500$ V/cm (blue solid curve), they are greatly damped at $F_{dc}=50$ V/cm (red dashed curve) due to an increased Bloch-oscillation period $T_B=2\pi/\omega_B \approx T_2$, where $\omega_B=eF_{dc}d/\hbar$ is the Bloch frequency. At the same time, however, the steady-state current is significantly enhanced. The above dependences of the magnitude of the steady-state current on the radius of the wire and F_{dc} will be studied in more detail in the following.

In Fig. 4, we study the steady-state current I_0 as a function of F_{dc} for different phonon and impurity scattering rates. The field scales as $1/d$. The results are consistent with the exact relaxation-time results obtained earlier by Lyo.[8] Figure 4(a) exhibits I_0 as a function of F_{dc} for two values of R. For a stronger phonon scattering with $R=10$ Å (solid squares on red curve), we first find a linear-transport behavior $I_0 \propto F_{dc}$ in the weak-field regime $F_{dc} \le 25$ V/cm corresponding to $\omega_B \ll \gamma_0, \gamma_{ph}$, where γ_{ph} represents the effective phonon-scattering rate [see the discussion of Fig. 6(a) below]. When $F_{dc} > 25$ V/cm, on the other hand, I_0 varies inversely with F_{dc} and evolves into a $1/\omega_B$ dependence for $F_{dc} \gg 25$ V/cm, where $\omega_B \gg \gamma_{ph}, \gamma_0$. At $F_{dc}=25$ V/cm, a sharp

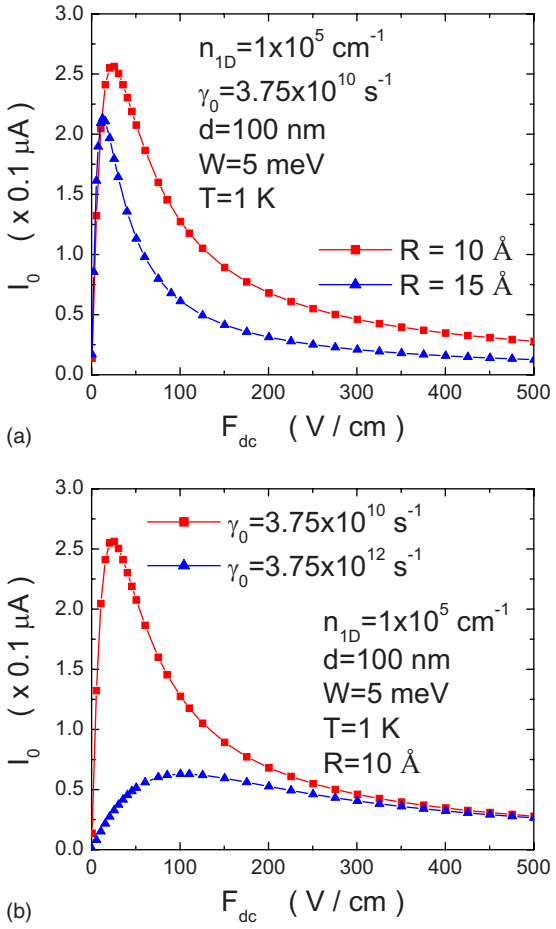

FIG. 4. (Color online) Calculated steady-state currents I_0 as functions of the dc electric field F_{dc} for two values of R [in (a)] and two values of γ_0 [in (b)]. We choose $R=10$ Å (solid squares on red curve) and $R=15$ Å (solid triangles on blue curve) in (a), while we assume $\gamma_0=3.75\times10^{10}$ s^{-1} (solid squares on red curve) and $\gamma_0=3.75\times10^{12}$ s^{-1} (solid triangles on blue curve) in (b). The other parameters are taken as the same as those in Fig. 2.

current peak is seen. When the phonon scattering is reduced with $R=15$ Å (solid triangles on blue curve), the peak current I_p is shifted to a lower field because the field F_p at the peak value of I_0 is proportional to γ_{ph} for small γ_0.[8] Moreover, the magnitude of I_p is also reduced since it is roughly proportional to γ_{ph}/γ_0.[8] Furthermore, the high-field current at $F_{dc}=500$ V/cm decreases when γ_{ph} is reduced, which can be attributed to the fact that the steady-state current is proportional to γ_{ph}/ω_B in the high-field limit $\omega_B \gg \gamma_0, \gamma_{ph}$.[8] We present in Fig. 4(b) I_0 as a function of F_{dc} for two values of γ_0. For a large $\gamma_0=3.75\times10^{12}$ s^{-1} (solid triangles on blue curve), the low-field I_0 is drastically reduced in comparison with that for a small $\gamma_0=3.75\times10^{10}$ s^{-1} (solid squares on red curve) because $I_0 \propto 1/\sqrt{\gamma_0}$ for $\gamma_0 \gg \gamma_{ph}$.[8] However, the high-field I_0 at $F_{dc}=500$ V/cm remains the same, independent of γ_0. In addition, F_p shifts to a high field because $F_p \propto \sqrt{\gamma_0}$ for $\gamma_0 \gg \gamma_{ph}$.[8] A report on the field dependence of tunneling current based on the Fokker-Planck approximation was given earlier in the absence of elastic scattering.[52]

In order to demonstrate the above discussed scaling relationships of I_p, F_p, and the high-field I_0 in the negative dif-

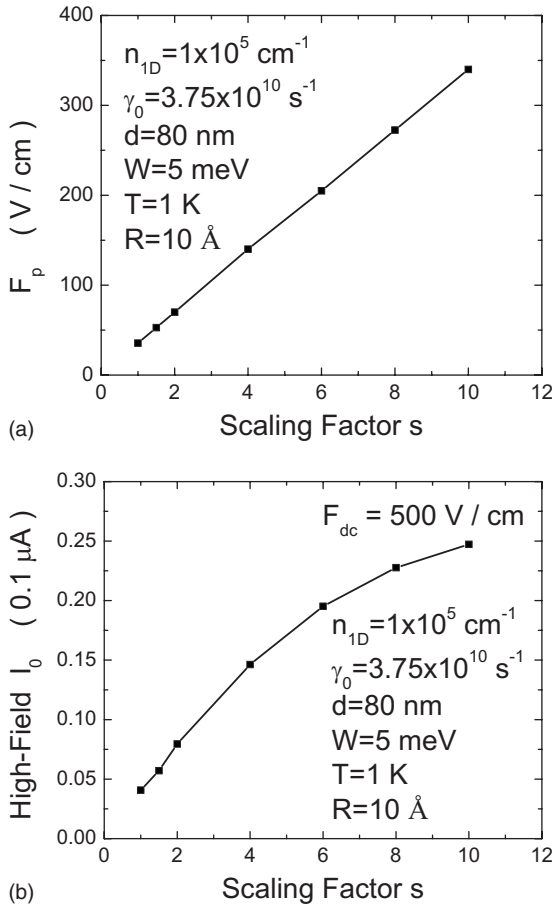

FIG. 5. Calculated field F_p at the peak of the steady-state current [in (a)] and the steady-state current I_0 at $F_{dc}=500$ V/cm [in (b)] as functions of the phonon interaction scaling factor s. The other parameters are taken as the same as those in Fig. 2 except for $d=80$ nm. The dimensionless scaling factor s in this figure measures the simple scaling relation, i.e., $|V_\lambda(\mathbf{q})|^2 \to s|V_\lambda(\mathbf{q})|^2$.

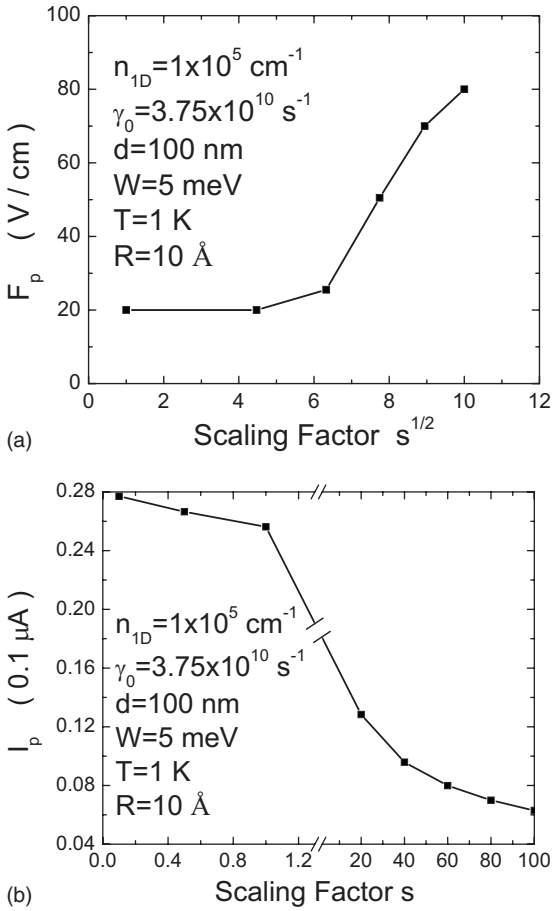

FIG. 6. Calculated peak field F_p [in (a)] and peak current I_p [in (b)] as functions of the impurity interaction scaling factor s. The other parameters are taken as the same as those in Fig. 2. The dimensionless scaling factor s in this figure measures the simple scaling relation, i.e., $\gamma_0 \to s\gamma_0$. The s scale in (b) has been broken to highlight the behavior of I_p for small values of s.

ferential conductance (NDC) regime with respect to γ_{ph} and γ_0, we introduce a dimensionless scaling parameter s by expressing the electron-phonon-scattering interaction using $|V_\lambda(\mathbf{q})|^2 \to s|V_\lambda(\mathbf{q})|^2$, where $|V_\lambda(\mathbf{q})|^2$ is given by Eq. (14) or through the replacement $\gamma_{ph} \to \bar{\gamma}_{ph} \equiv s\gamma_{ph}$. Figure 5(a) displays F_p as a function of s for a small γ_0. A linear dependence was found, which implied that F_p in this case, is proportional to $\bar{\gamma}_{ph}$ under the condition $\bar{\gamma}_{ph} \gg \gamma_0$.[8] This relationship is consistent with our previous analytical result based on the relaxation-time approximation. Figure 5(b) shows the high-field steady-state current I_0 as a function of s and demonstrates that I_0 increases with $\bar{\gamma}_{ph}$ linearly for small $\bar{\gamma}_{ph}$, but nonlinearly for large $\bar{\gamma}_{ph}$. Again, this behavior is consistent with the predictions of our previous exact result.[8] Therefore, the nonlinear-dependence region in Fig. 5(b) reflects a switching behavior from the strong-field regime ($\omega_B \gg \bar{\gamma}_{ph}$) to the weak-field regime ($\omega_B \ll \bar{\gamma}_{ph}$).

For impurity scattering, we can also introduce a dimensionless scaling factor s through $\gamma_0 \to \bar{\gamma}_0 \equiv s\gamma_0$. Figure 6(a) exhibits F_p as a function of $\sqrt{s}$. We find from the figure that F_p increases as $F_p \propto \sqrt{\bar{\gamma}_0}$ with $\bar{\gamma}_0$ for large $\bar{\gamma}_0$, but becomes independent of $\bar{\gamma}_0$ for small $\bar{\gamma}_0$. This confirms our previous analytical result[8] which predicts that F_p is equal to $(\hbar/ed)\sqrt{\gamma_{ph}(\gamma_{ph}+\bar{\gamma}_0)}$. Therefore, the constant value in Fig. 6(a) as $\bar{\gamma}_0 \to 0$ corresponds to $\hbar\gamma_{ph}/ed$, from which we can extract the value of effective phonon-scattering rate $\gamma_{ph} \sim 3 \times 10^{11}$ s^{-1}. We show I_p in Fig. 6(b) as a function of s, which exhibits a decrease in I_p with increasing $\bar{\gamma}_0$ for large $\bar{\gamma}_0$, and approaches a constant with decreasing $\bar{\gamma}_0$ for small $\bar{\gamma}_0$. This again confirms our previous analytical result[8] which predicts that I_p is equal to $(e\hbar n_{1D}/4m^*_{eff}d)\sqrt{\gamma_{ph}/(\gamma_{ph}+\bar{\gamma}_0)}$.

Figure 7(a) displays $I_{1D}(t)$ for two temperatures T at a high dc field $F_{dc}=500$ V/cm. In comparison with the result at $T=1$ K (red solid curve), the increased temperature $T=20$ K (blue dashed curve) only reduces the amplitude of the Bloch oscillations but does not change the oscillation period. In addition, the steady-state current also decreases with increasing T. We show in Fig. 7(b) the steady-state current I_0 as a function of F_{dc} for two temperatures. Compared with the result at $T=1$ K (solid squares on red curve), I_0 becomes smaller for the higher temperature $T=20$ K (solid triangles on blue curve).

To compare the different T dependences of I_0 in the linear-response and the high-field NDC regime, we display I_0

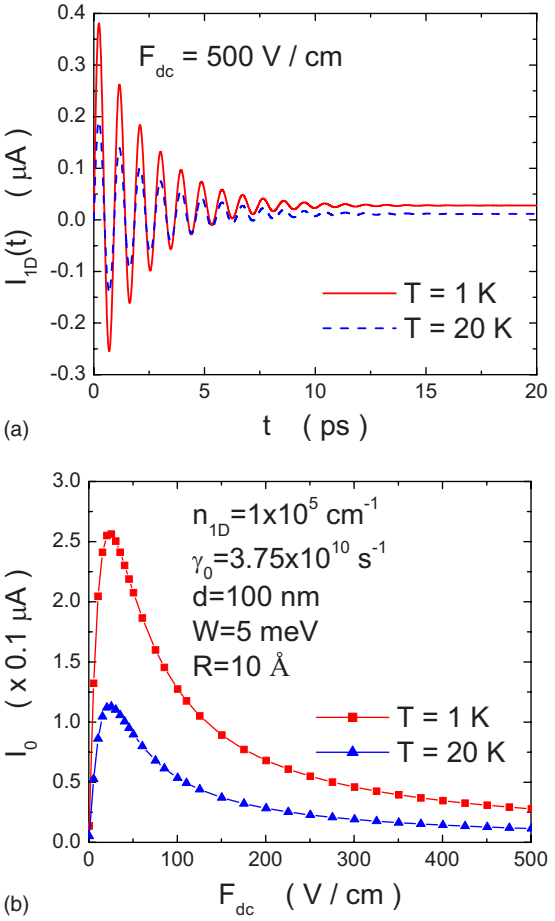

FIG. 7. (Color online) Calculated transient currents $I_{1D}(t)$ at $F_{dc}=500$ V/cm as a function of t [in (a)] for two values of the temperature, i.e., $T=1$ K (red solid curve) and $T=20$ K (blue dashed curve) and the steady-state current I_0 as a function of F_{dc} [in (b)] for two values of the temperature, i.e., $T=1$ K (solid squares on red curve) and $T=20$ K (solid triangles on blue curve). The other parameters are taken as the same as those in Fig. 2.

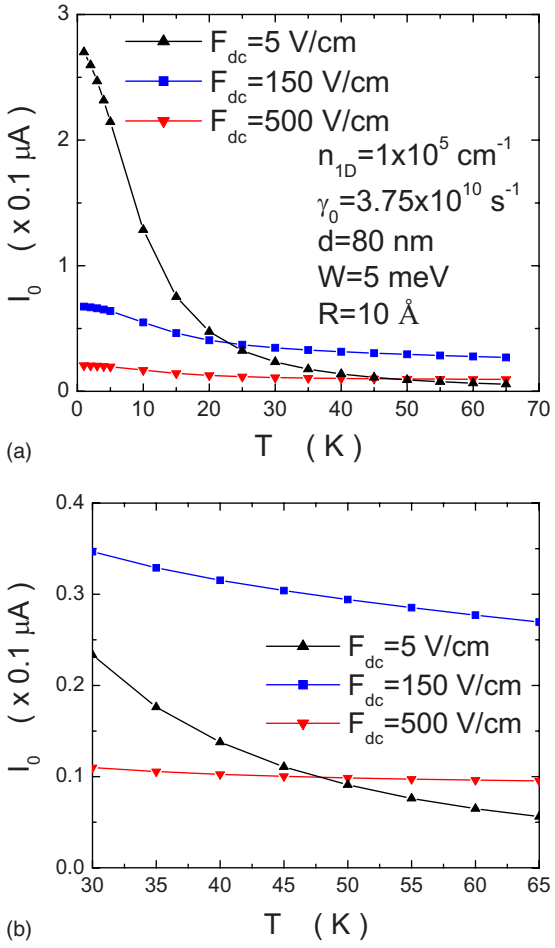

FIG. 8. (Color online) Calculated steady-state currents I_0 as functions of the temperature [in (a)] for three values of F_{dc}, i.e., $F_{dc}=5$ V/cm, $F_{dc}=150$ V/cm, and $F_{dc}=500$ V/cm correspond to solid triangles on black, solid squares on blue, and inverted solid triangles on red curves, respectively. A blowout view of the curves in (a) is presented in (b) for $30 \leq T \leq 65$ K to highlight the high-temperature behaviors. Here, we take $d=80$ nm, and the other parameters are taken as the same as those in Fig. 2.

in Fig. 8(a) as a function of T for $F_{dc}=5$ V/cm (solid triangles on black curve), $F_{dc}=150$ V/cm (solid squares on blue curve), and $F_{dc}=500$ V/cm (inverted solid triangles on red curve), respectively. In the linear-response regime at $F_{dc}=5$ V/cm, I_0 decreases rapidly at low temperatures with increasing T as well known due to electron-phonon scattering. This rapid drop is visibly slowed down in the low-field NDC regime for $F_{dc}=150$ V/cm with much smaller low-temperature values of I_0. For $F_{dc}=500$ V/cm in the high-field NDC regime, the low-temperature values of I_0 are further reduced. More importantly, I_0 becomes nearly independent of T at high temperatures. This T-independent behavior at $F_{dc}=500$ kV/cm can be seen more clearly in Fig. 8(b), where I_0 is plotted within the small range of $30 \leq T \leq 65$ K. This T-independent behavior in the NDC regime is consistent with previous findings in one dimension[8] and three dimensions.[53,54]

B. Damped dynamical localization

In the coexistence of dc and ac fields, electrons execute simultaneous drift and oscillatory motion. Figure 9(a) presents calculated time-dependent currents $I_{1D}(t)$ for three values of $F_{ac}=100$ V/cm (brown dashed curve), $F_{ac}=300$ V/cm (red dashed-dotted curve), and $F_{ac}=500$ V/cm (blue solid curve) at $F_{dc}=30$ V/cm and $\nu_{ac}=0.1$ THz. The ac current establishes regular periodic oscillations quickly in a time scale larger than the scattering time, which roughly corresponds to $\nu_{ac}t=0.3$ shown in Fig. 9: the time interval between each period here is 10 ps, while the relaxation (scattering) time is about 0.3 ps. For $F_{ac}=100$ V/cm, $I_{1D}(t)$ largely follows the wave profile of $\cos(2\pi\nu_{ac}t)$ except for some small distortions. However, when F_{ac} is increased to 500 V/cm, significant higher harmonics, such as $2\nu_{ac}, 3\nu_{ac}, \ldots$, can be seen from damped fast oscillations superposed on the shoulders between minima and maxima that occur for $F_{ac}=100$ V/cm. This is attributed to the increase in the argument of the mth-order Bessel function $J_m(eF_{ac}d/h\nu_{ac})$.[36,38] Here, $m=0,1,2,\ldots$ is an integer labeling an m-photon-assisted tunneling process.[55] We display in Fig. 9(b) $I_{1D}(t)$ for $F_{dc}=0$ (blue dashed curve) and F_{dc}

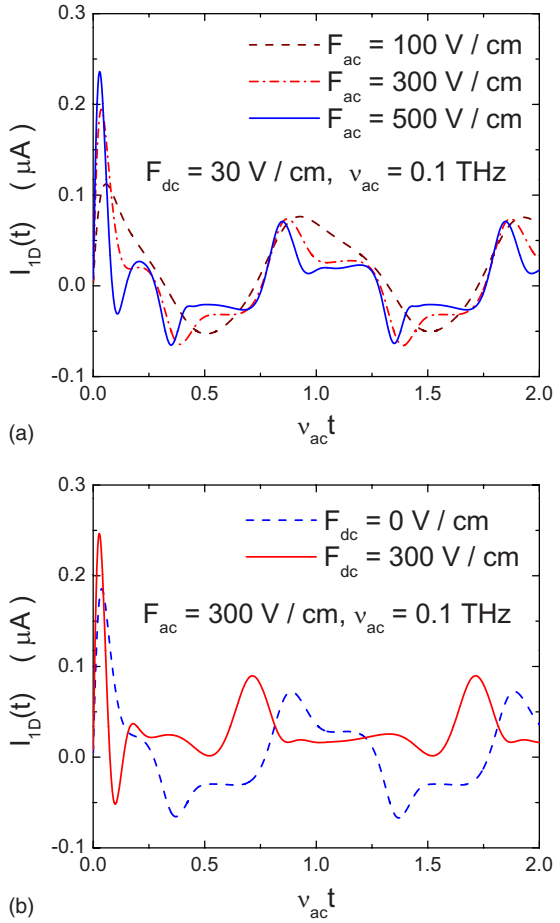

FIG. 9. (Color online) Calculated transient currents $I_{1D}(t)$ as functions of the scaled time $\nu_{ac}t$ for three different amplitudes F_{ac} of an applied ac electric field [in (a)], and for with/without a dc electric field [in (b)]. In (a) we set $F_{dc}=30$ V/cm and display the results for $F_{ac}=100$ (brown dashed curve), $F_{ac}=300$ (red dashed-dotted curve), and $F_{ac}=500$ V/cm (blue solid curve), while in (b) we take $F_{ac}=300$ V/cm and present the results for $F_{dc}=0$ (blue dashed curve) and $F_{dc}=300$ V/cm (red solid curve). Here, we set $\nu_{ac}=0.1$ THz, $n_{1D}=1\times10^5$ cm^{-1}, $\gamma_0=3.75\times10^{12}$ s^{-1}, $d=80$ nm, $W=5$ meV, $T=1$ K, and $R=10$ Å.

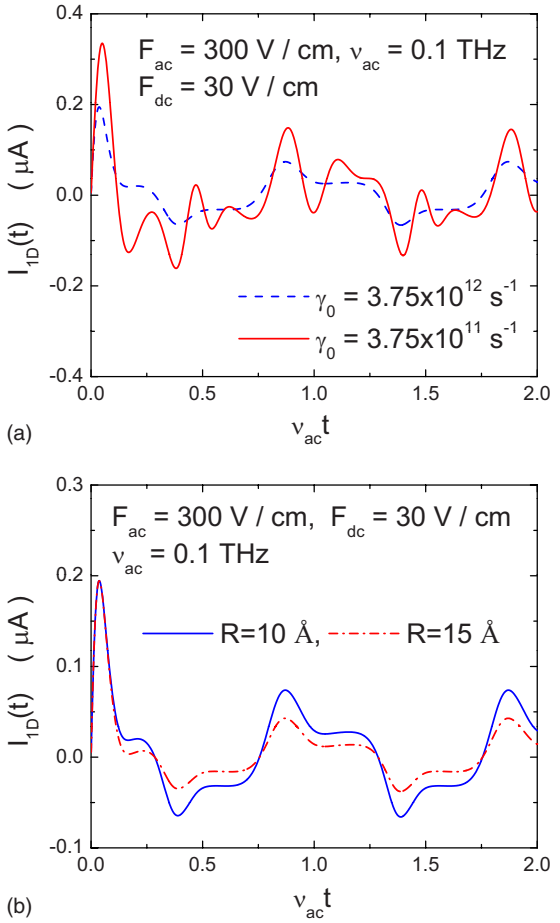

FIG. 10. (Color online) Calculated transient currents $I_{1D}(t)$ as functions of $\nu_{ac}t$ for two values of γ_0 [in (a)] and two values of R [in (b)] with $F_{dc}=30$ V/cm and $F_{ac}=300$ V/cm. We choose $\gamma_0=3.75\times10^{12}$ s^{-1} (blue dashed curve) and $\gamma_0=3.75\times10^{11}$ s^{-1} (red solid curve) in (a), while we assume $R=10$ Å (blue solid curve) and $R=15$ Å (red dashed-dotted curve) in (b). The other parameters are taken as the same as those in Fig. 9.

$=300$ V/cm (red solid curve) at $F_{ac}=300$ V/cm and $\nu_{ac}=0.1$ THz. Compared with the result at $F_{dc}=0$, there exists a rigid phase shift for $F_{dc}=300$ V/cm, in addition to the suppression of minima that occur for $F_{dc}=0$. In this case, asymmetry is introduced by a finite dc electric field, which has a profound effect on time-averaged currents. In fact, the time-averaged current remains to be zero for all values of F_{ac} and ν_{ac} in the absence of drift at $F_{dc}=0$, reflecting the purely oscillating ac current.

Figure 10(a) compares the calculated transient currents $I_{1D}(t)$ for $\gamma_0=3.75\times10^{12}$ s^{-1} (blue dashed curve) and $\gamma_0=3.75\times10^{11}$ s^{-1} (red solid curve) at $F_{dc}=30$ V/cm, $F_{ac}=300$ V/cm, and $\nu_{ac}=0.1$ THz. When γ_0 is increased to 3.75×10^{12} s^{-1}, the fast oscillations associated with higher harmonics are quickly quenched by elastic scattering of electrons along with a reduced peak strength, giving rise to a partial recovery of the result under a weak F_{ac} [see the brown dashed curve in Fig. 9(a)]. Figure 10(b) presents $I_{1D}(t)$ for $R=10$ Å (blue solid curve) and $R=15$ Å (red dashed-dotted curve) at $F_{dc}=30$ V/cm, $F_{ac}=300$ V/cm, and $\nu_{ac}=0.1$ THz. In this case, however, we find that the increased phonon scattering with $R=10$ Å only enhances the magnitude of the oscillation peaks, but the phase of $I_{1D}(t)$ remains unchanged. Therefore, the inelastic phonon scattering of electrons stabilizes the higher harmonics induced by $F_{ac}=300$ V/cm. The so-called dynamical localization occurs whenever the quantity $x\equiv eF_{ac}d/h\nu_{ac}$ becomes the root $x_j^{(m)}$ of $J_m(x)$, where $j=1,2,\ldots$ labels the roots. Physically speaking, the dynamical-localization phenomenon can be regarded as the continued localization of an initially localized wave packet.[38] This can be reflected in the zeros of the calculated time-averaged current $\langle I_{1D}\rangle$ for some specific values of F_{ac} or $1/\nu_{ac}$.

We compare in Fig. 11(a) the calculated time-averaged currents $\langle I_{1D}\rangle$ as a function of $1/\nu_{ac}$ for three values of $F_{ac}=100$ V/cm (solid squares on red curve), $F_{ac}=300$ V/cm (solid triangles on green curve), and $F_{ac}=500$ V/cm (inverted solid triangles on blue curve) at $F_{dc}=30$ V/cm. The sign of $\langle I_{1D}\rangle$ here is determined by the signs of F_{ac} and F_{dc}.

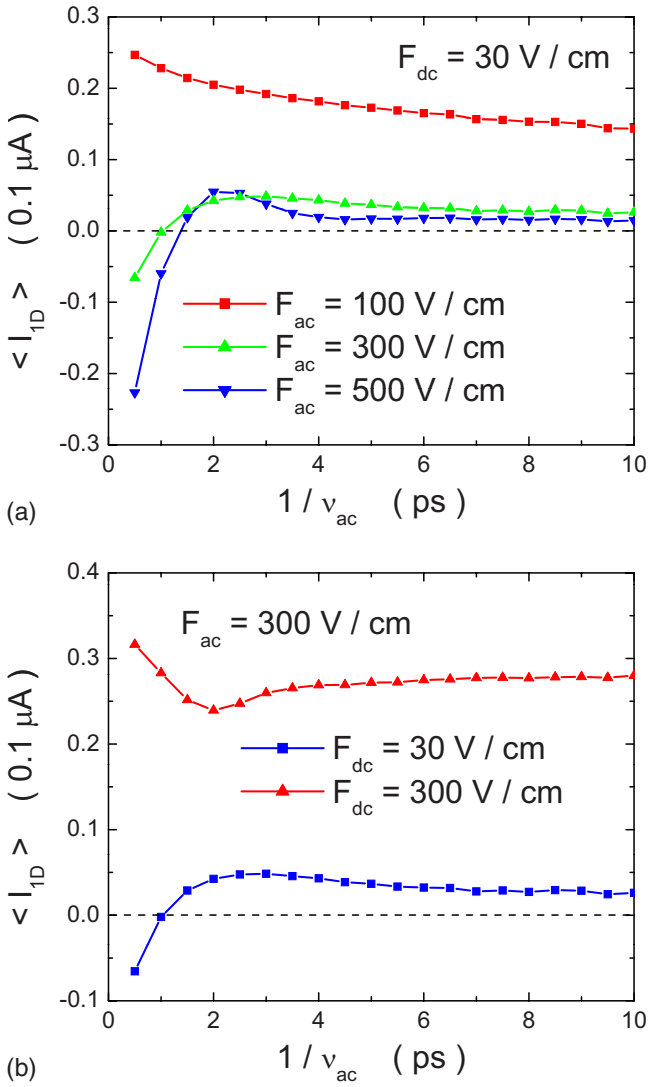

FIG. 11. (Color online) Calculated long-time average currents $\langle I_{1D}\rangle$ as functions of inverse frequency $1/\nu_{ac}$ for three values of F_{ac} [in (a)] and two values of F_{dc} [in (b)]. We choose $F_{ac}=100$ V/cm (solid squares on red curve), $F_{ac}=300$ V/cm (solid triangles on green curve), and $F_{ac}=500$ V/cm (inverted solid triangles on blue curve) in (a), while we assume $F_{dc}=30$ V/cm (solid squares on blue curve) and $F_{dc}=300$ V/cm (solid triangles on red curve) in (b). The horizontal black dashed lines are used as a guideline for $\langle I_{1D}\rangle=0$. The other parameters are taken as the same as those in Fig. 9 except for $F_{dc}=30$ V/cm in (a) and $F_{ac}=300$ V/cm in (b).

Here, the point of intersection of each curve with the horizontal dashed line for a large value of F_{ac} represents the first root $x_1^{(m)}$ of $J_{|m|}(eF_{ac}d/h\nu_{ac})$ for different values of $|m|$.[36,38] When F_{ac} is reduced, the intersection point moves leftward due to decreasing $x_1^{(m)}$ with a smaller and smaller $|m|$ value. As the last intersection point $x_1^{(0)}$ is passed for $F_{ac}=100$ V/cm, the point of intersection vanishes, and the dynamical localization in this case becomes completely suppressed. Once the intersection point is passed, $\langle I_{1D}\rangle$ becomes more and more negative with decreasing $1/\nu_{ac}$. On the other hand, for large values of F_{ac}, the magnitude of $\langle I_{1D}\rangle$ is greatly reduced and approaches zero in the large $1/\nu_{ac}$ regime. This is a consequence of decreasing $|J_m(x)|$ with increasing x for all values of m:

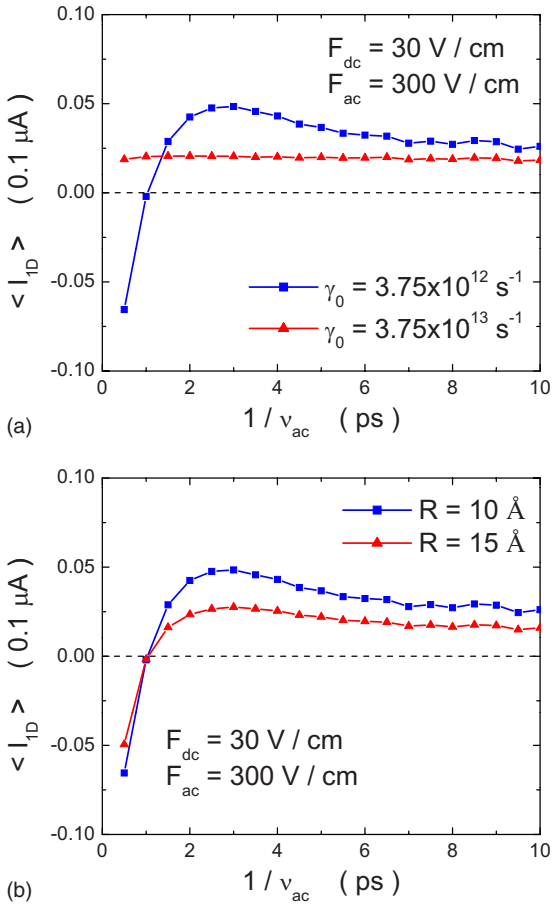

FIG. 12. (Color online) Calculated long-time average currents $\langle I_{1D}\rangle$ as functions of $1/\nu_{ac}$ for two values of γ_0 [in (a)] and two values of R [in (b)] with $F_{dc}=30$ V/cm and $F_{ac}=300$ V/cm. We choose $\gamma_0=3.75\times10^{12}$ s^{-1} (solid squares on blue curve) and $\gamma_0=3.75\times10^{13}$ s^{-1} (solid triangles on red curve) in (a), while we assume $R=10$ Å (solid squares on blue curve) and $R=15$ Å (solid triangles on red curve) in (b). The horizontal black dashed lines are used as a guideline for $\langle I_{1D}\rangle=0$. The other parameters are taken as the same as those in Fig. 9.

$$J_m(x)=\sqrt{\frac{2}{\pi x}}\cos\left(x-\frac{1}{2}m\pi-\frac{1}{4}\pi\right)\ ,\ x=\frac{eF_{ac}d}{h\nu_{ac}}\gg 1.$$

Figure 11(b) presents $\langle I_{1D}\rangle$ as a function of $1/\nu_{ac}$ at $F_{ac}=300$ V/cm for $F_{dc}=30$ V/cm (solid squares on blue curve) and $F_{dc}=300$ V/cm (solid triangles on red curve). For $F_{dc}=300$ V/cm, there is no intersection point. In this case, the strong Bloch oscillations under $F_{dc}=300$ V/cm completely suppress the dynamical localization. For a large value of $1/\nu_{ac}$, the magnitude of $\langle I_{1D}\rangle$ will eventually approach a value ($\sim 1/\omega_B$) determined by $F_{dc}=300$ V/cm, in contrast with a very small value under $F_{dc}=30$ V/cm. In the latter case, the dominant contribution to $\langle I_{1D}\rangle$ comes from the term containing $J_1(eF_{ac}d/h\nu_{ac})$.[36] For a large F_{dc}, on the other hand, the dominant contribution to $\langle I_{1D}\rangle$ is from the term containing $J_0(eF_{ac}d/h\nu_{ac})$.[36] Therefore, $\langle I_{1D}\rangle$ is deter-

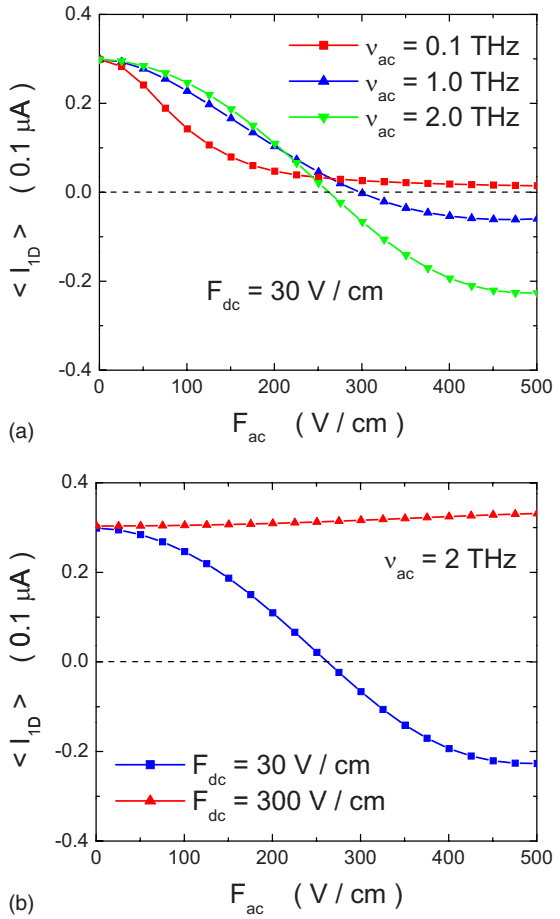

FIG. 13. (Color online) Calculated long-time average currents $\langle I_{1D}\rangle$ as functions of the amplitude of an ac-field component F_{ac} for three values of ν_{ac} [in (a)] and two values of F_{dc} [in (b)]. We choose $\nu_{ac}=0.1$ THz (solid squares on red curve), $\nu_{ac}=1$ THz (solid triangles on blue curve), and $\nu_{ac}=2$ THz (inverted solid triangles on green curve) in (a), while we assume $F_{dc}=30$ (solid squares on blue curve) and $F_{dc}=300$ V/cm (solid triangles on red curve) in (b). The horizontal black dashed lines are used as a guideline for $\langle I_{1D}\rangle=0$. The other parameters are taken as the same as those in Fig. 9 except for $F_{dc}=30$ V/cm in (a) and $\nu_{ac}=2$ THz in (b).

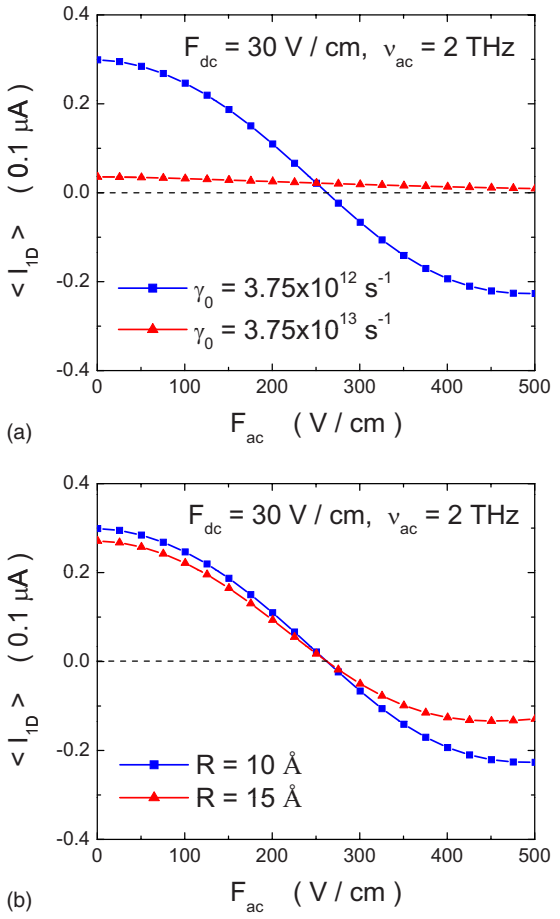

FIG. 14. (Color online) Calculated long-time average currents $\langle I_{1D}\rangle$ as functions of F_{ac} for two values of γ_0 [in (a)] and two values of R [in (b)] with $F_{dc}=30$ V/cm and $\nu_{ac}=2$ THz. We choose $\gamma_0=3.75\times10^{12}$ s^{-1} (solid squares on blue curve) and $\gamma_0=3.75\times10^{13}$ s^{-1} (solid triangles on red curve) in (a), while we assume $R=10$ Å (solid squares on blue curve) and $R=15$ Å (solid triangles on red curve) in (b). The horizontal black dashed lines are used as a guideline for $\langle I_{1D}\rangle=0$. The other parameters are taken as the same as those in Fig. 9.

mined by $J_0(eF_{ac}d/h\nu_{ac})$ for a large F_{dc} and by $J_1(eF_{ac}d/h\nu_{ac})$ for a small F_{dc}.

We show in Fig. 12(a) a comparison of $\langle I_{1D}\rangle$ as a function of $1/\nu_{ac}$ at $F_{dc}=30$ V/cm and $F_{ac}=300$ V/cm for $\gamma_0=3.75\times10^{12}$ s^{-1} (solid squares on blue curve) and $\gamma_0=3.75\times10^{13}$ s^{-1} (solid triangles on red curve). Here, the increased impurity scattering of electrons kills the dynamical-localization features completely. Figure 12(b) compares $\langle I_{1D}\rangle$ as a function of $1/\nu_{ac}$ for $R=10$ Å (solid squares on blue curve) and $R=15$ Å (solid triangles on red curve) at $F_{dc}=30$ V/cm and $F_{ac}=300$ V/cm. Remarkably, the increased phonon scattering with $R=10$ Å in this case not only leaves the intersection points unchanged, but also increases the magnitude of the oscillation peaks in the small $1/\nu_{ac}$ regime, as seen from Fig. 10(b). We must emphasize that phonon scattering plays a complete opposite role on the dynamical localization in comparison with impurity scattering.

Figure 13(a) presents $\langle I_{1D}\rangle$ as a function of F_{ac} for three different values of ν_{ac} at $F_{dc}=30$ V/cm, where $\nu_{ac}=0.1$ THz (solid squares on red curve), $\nu_{ac}=1$ THz (solid triangles on blue curve), and $\nu_{ac}=2$ THz (inverted solid triangles on green curve). Here, the intersection point $x_1^{(m)}$ for different values of $|m|$ moves leftward with increasing ν_{ac} due to decreasing $x_1^{(m)}$ with a smaller and smaller $|m|$ value. The explanation for this is similar to that given in Fig. 11(a). The values of $\langle I_{1D}\rangle$ for different ν_{ac} becomes the same as $F_{ac}=0$. Moreover, $\langle I_{1D}\rangle$ becomes more and more negative in the high-F_{ac} regime when ν_{ac} increases due to enhanced $|J_m(eF_{ac}d/h\nu_{ac})|$ with a large value of ν_{ac}. In Fig. 13(b), two results for $\langle I_{1D}\rangle$ are compared as a function of F_{ac} at $\nu_{ac}=2$ THz for $F_{dc}=30$ V/cm (solid squares on blue curve) and $F_{dc}=300$ V/cm (solid triangles on red curve). At $F_{dc}=300$ V/cm, there exists no intersection point anymore, and the dynamical localization in this case becomes completely suppressed by strong Bloch oscillations. For $F_{ac}=0$, the two values of the dc current $\langle I_{1D}\rangle$ for $F_{dc}=30$ and 300 V/cm are accidentally close as seen from the solid triangles on blue

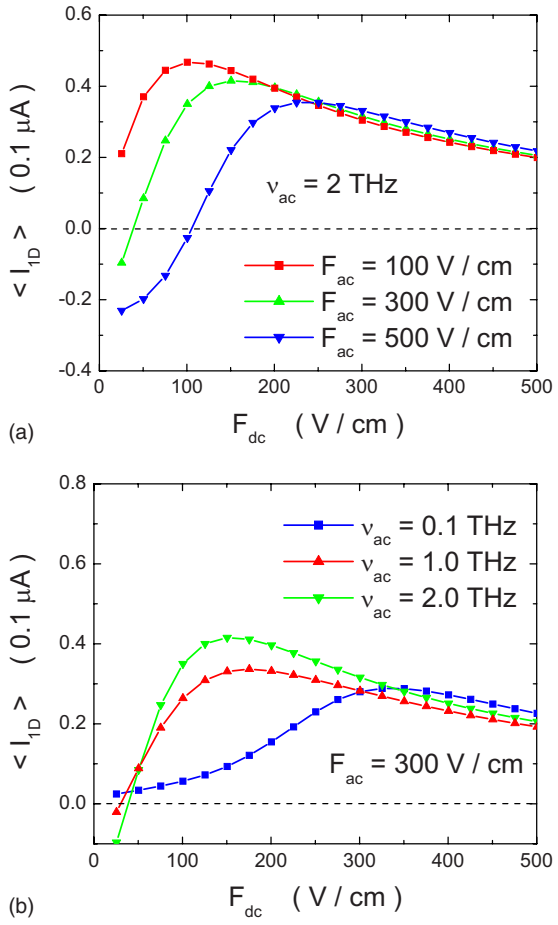

FIG. 15. (Color online) Calculated long-time average currents $\langle I_{1D}\rangle$ as functions of the amplitude of a dc-field component F_{dc} for three values of F_{ac} [in (a)] and three values of ν_{ac} [in (b)]. We choose $F_{ac}=100$ V/cm (solid squares on red curve), $F_{ac}=300$ V/cm (solid triangles on green curve), and $F_{ac}=500$ V/cm (inverted solid triangles on blue curve) in (a), while we assume $\nu_{ac}=0.1$ THz (solid squares on blue curve), $\nu_{ac}=1$ THz (solid triangles on red curve) and $\nu_{ac}=2$ THz (inverted solid triangles on green curve) in (b). The other parameters are taken as the same as those in Fig. 9 except for $\nu_{ac}=2$ THz in (a) and $F_{ac}=300$ V/cm in (b). The horizontal black dashed lines are used as a guideline for $\langle I_{1D}\rangle=0$.

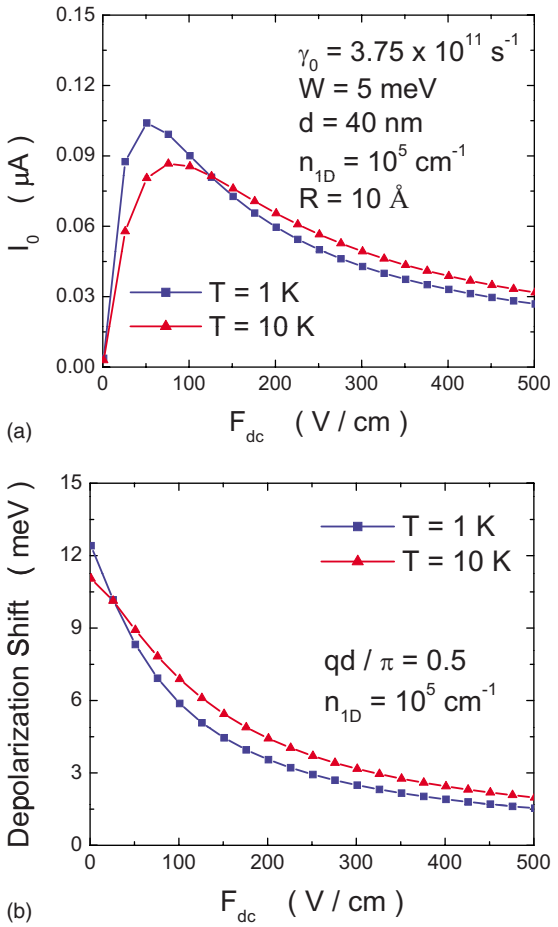

FIG. 16. (Color online) (a) Steady-state current I_0 as a function of dc electric field F_{dc}. (b) Depolarization shift $\mathcal{D}(q)$ as a function of F_{dc} with $qd=\pi/2$. The temperatures chosen are $T=1$ K (solid squares on blue curves) and $T=10$ K (solid triangles on red curves). The parameters used in these calculations are: $n_{1D}=10^5$ cm^{-1}, $\gamma_0=3.75\times10^{11}$ sec^{-1}, $d=40$ nm, $W=5$ meV, and $R=10$ Å.

curve in Fig. 4(b), one sitting in the nearly linear-response regime and the other in the NDC regime.

Calculated results for $\langle I_{1D}\rangle$ are compared for $\gamma_0=3.75\times10^{12}$ s^{-1} (solid squares on blue curve) and $\gamma_0=3.75\times10^{13}$ s^{-1} (solid triangles on red curve) in Fig. 14(a) as a function of F_{ac} with $F_{dc}=30$ V/cm and $\nu_{ac}=2$ THz. Here, the increased impurity scattering makes the intersection point (i.e., the dynamical localization) disappear from the shown F_{ac} region, and the magnitude of the oscillations is greatly suppressed. We display in Fig. 14(b) $\langle I_{1D}\rangle$ as a function of F_{ac} for $R=10$ Å (solid squares on blue curve) and $R=15$ Å (solid triangles on red curve) at $F_{dc}=30$ V/cm and $\nu_{ac}=2$ THz. The enhanced phonon scattering with $R=10$ Å only slightly increases the magnitude of the oscillation peak but leaves the intersection point unshifted. This again demonstrates the opposite roles played by elastic and inelastic scattering of electrons, respectively, on the dynamical localization of the current system.

A comparison of the results for the calculated $\langle I_{1D}\rangle$ is given in Fig. 15(a) as a function of the amplitude of F_{dc} for $F_{ac}=100$ V/cm (solid squares on red curve), $F_{ac}=300$ V/cm (solid triangles on green curve) and $F_{ac}=500$ V/cm (inverted solid triangles on blue curve), where $\nu_{ac}=2$ THz is assumed. In the limit of $F_{ac}=0$, this becomes the I-V curve studied earlier. A dc-field-induced Esaki-Tsu peak[1] is gradually built up at a dc field F_{dc} which decreases with decreasing F_{ac}: the dynamical-localization intersection point moves to the left at the same time. Moreover, the negative minimum also shifts to the left, disappearing at $F_{dc}=0$. There is only one Esaki-Tsu-type peak in this figure, which qualitatively agrees with the early experimental observation by Winnerl *et al.*[56] Eventually, the three $\langle I_{1D}\rangle$ curves for different values of F_{ac} merge into one for large F_{dc}, and the dynamical localization in the system is completely suppressed by the strong Bloch oscillations. The results for $\langle I_{1D}\rangle$ are presented as a function of F_{dc} in Fig. 15(b) for $\nu_{ac}=0.1$ THz (solid squares on blue curve), $\nu_{ac}=1$ THz (solid

triangles on red curve), and $\nu_{ac}=2$ THz (inverted solid triangles on green curve) and for $F_{ac}=300$ V/cm. Here, the negative minimum is completely suppressed when ν_{ac} reduces to 0.1 THz. At the same time, the Esaki-Tsu-type peak is pushed to a high dc field for $\nu_{ac}=0.1$ THz. Again, $\langle I_{1D}\rangle$ curves for three values of ν_{ac} merge into one as F_{dc} becomes very large.

C. dc-field-driven optical absorption

In Fig. 16(a), we plot the tunneling current I_0 [see its definition after Eq. (34)] as a function of the applied dc electric field F_{dc} for $T=1$ K (solid squares on blue curve) and $T=10$ K (solid triangles on red curve). When F_{dc} is small, the $I_0 \propto F_{dc}$ Ohm's law is obeyed in the low-field regime, similar to Fig. 7(b). The phonon-scattering rate is enhanced as the temperature is increased. Consequently, I_0 is reduced, as expected, at low electric fields. In addition, when F_{dc} is large, an inverse law behavior $I_0 \propto 1/F_{dc}$ is observed in the NDC regime after passing through the Esaki-Tsu peak.[1] However, in this range of high applied dc electric field, I_0 unexpectedly increases with T because the increased phonon-scattering rate has been overcome by the role played by the reduction in the center of mass ($\propto 1/d$), as explained by Lyo,[8] which is different from the result in Fig. 7(b) with a larger value of d. In Fig. 16(b), we compare the depolarization shift $\mathcal{D}(q)$ at $qd=\pi/2$ as a function of F_{dc} for $T=1$ K and $T=10$ K. As seen from Eq. (42), the dependence of $\mathcal{D}(q)$ on F_{dc} comes from the amplitude prefactor $\mathcal{A}[F_{dc}]$, which decreases monotonically with increasing F_{dc} due to piling up of electrons at one of the Brillouin-zone boundaries at $k=-\pi/d$. When F_{dc} is small, $f_k \approx f_k^{(0)}$. Consequently, $\mathcal{D}(q)$ decreases with increasing T in the low-field range due to increased thermal population of large-k states with a higher kinetic energy. When F_{dc} is large in the NDC regime, however, $\mathcal{D}(q)$ increases with T due to an anomalous enhancement of $\mathcal{A}[F_{dc}]$ by nonlinear electrons, as explained for Fig. 16(a).

We compare in Fig. 17(a) the peak energies $[\hbar q v_d + \mathcal{D}(q)]$ for fixed $qd=\pi/2$ as a function of F_{dc} at two temperatures $T=1$ K and $T=10$ K. It is clear from Fig. 17(a) that the many-body depolarization shift, $\mathcal{D}(q)$, dominates the Doppler shift, $\hbar q v_d$, in the whole range of F_{dc} except when $F_{dc} \leq 50$ V/cm. For $F_{dc} \leq 50$ V/cm, there is a plateau in the peak energy which is due to the compensation from the linear reduction in v_d with decreasing F_{dc} in this low-field limit. From Fig. 17(b) we further find that the peak strength, which is proportional to $\sqrt{\mathcal{A}[F_{dc}]}$, decreases with increasing F_{dc} in addition to an anomalous enhancement by nonlinear electronic effects within the NDC regime at a higher temperature.

Our result in Eq. (40) shows that the peak strength is $\propto \sin(qd/2)/q^2$, which scales as $\sim 1/q$ for small q. In Fig. 18(a) we set at $T=1$ K. We see that there is a dramatic enhancement of the peak strength when q is reduced. However, $\mathcal{D}(q) \propto \sin(qd/2)$ and at $T=1$ K, shown in Fig. 18(b), is reduced for a smaller value of q (solid triangles on red curve).

IV. CONCLUSIONS

We presented numerical results for the time-dependent and steady-state currents in a strong nonlinear dc electric field for an electron gas in a 1D quantum-dot superlattice. A microscopic model was employed for the scattering of electrons by phonons and static impurities within the framework of the Boltzmann equation. For the steady-state I-V curves, we studied the scaling relations between the strengths of elastic, inelastic scattering and the peak current, the electric field at the peak current, and the high-field current in the NDC regime. The scaling results are very similar to those predicted by the recent exact analytic treatment based on a relaxation-time model for electron-phonon scattering.[8] The results demonstrate different roles played by elastic and inelastic scattering on the damped Bloch oscillations and the nonlinear steady-state current.

We have also calculated the time-dependent current and the long-time-averaged current under a nonlinear ac field via the same model. The results demonstrate opposite roles played by elastic and inelastic scattering on the damped dynamical localization. While elastic scattering suppresses dynamical localization at all frequencies, inelastic scattering has no effect on dynamical localization. Furthermore, it enhances the ac current amplitude at high frequencies. Effects of the combined ac and dc fields on the current were also

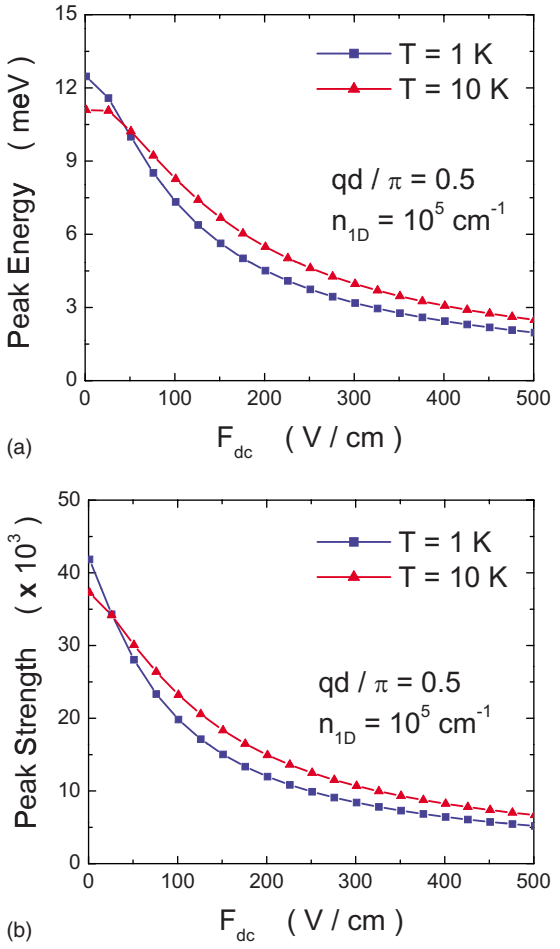

FIG. 17. (Color online) (a) Peak energies $[\hbar q v_d + \mathcal{D}(q)]$ and (b) relative peak strengths at $qd=\pi/2$ as functions of F_{dc} at $T=1$ K (solid squares on blue curves) and $T=10$ K (solid triangles on red curves). The other parameters used in these calculations are the same as in Fig. 16.

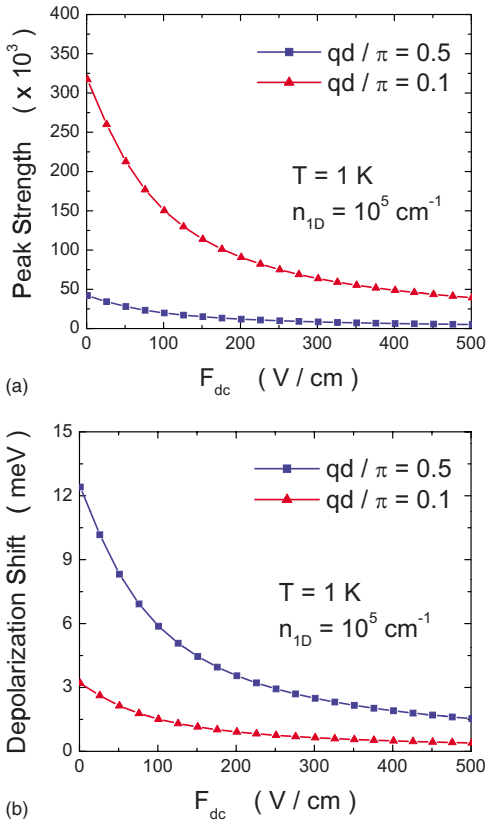

FIG. 18. (Color online) (a) Relative peak strengths and (b) depolarization shifts at $T=1$ K as functions of F_{dc} for $qd=\pi/2$ (solid squares on blue curves) and $qd=\pi/10$ (solid triangles on red curves). The other parameters used in these calculations are the same as in Fig. 16.

studied. We found a suppression of dynamical localization by strong Bloch oscillations and features in the Esaki-Tsu peaks under a finite ac electric field in the presence of electron scattering. Finally, we also studied the ac response of the current under the composite field $F(t)=F_{dc}+F_{ac}\cos(2\pi\nu_{ac}t+\phi)$ by varying the phase ϕ. The phase dependence was found to be very weak.

On the basis of calculated nonequilibrium electron distribution from the Boltzmann equation, we were further employ a self-consistent-field approach which in turn established a general formalism for the optical response of driven nonequilibrium electrons in the presence of a bias field which is allowed to be strong.

Within the framework of the developed theory, we have investigated the dependence on dc field of the peak energy and the peak strength in the absorption spectrum, for current-driven nonequilibrium electrons in a 1D quantum-dot superlattice at various temperatures and with different probe-field wave numbers. Both the peak energy and peak strength have been found to be reduced with increasing dc field. Our calculations have further demonstrated the following: (1) the peak energy and peak strength are both reduced when the temperature is increased for the linear transport of electrons; (2) the peak energy and peak strength are enhanced by raising the temperature for the nonlinear transport of electrons.

ACKNOWLEDGMENTS

One of the authors (S.K.L.) wishes to thank Wei Pan for valuable discussions. Sandia is a multiprogram laboratory operated by Sandia Corporation, a Lockheed Martin Co., for the U.S. DOE under Contract No.DE-AC04-94AL85000. D.H. would like to thank the Air Force Office of Scientific Research (AFOSR) for its support. G.G. was supported by AFRL under Contract No. FA 9453-07-C-0207.

APPENDIX A: TIGHT-BINDING WAVE FUNCTION

The tight-binding wave function of electrons in a 1D quantum-dot superlattice in the x direction can be written as[28]

$$\Psi_k(\vec{r})=\alpha(\rho)\frac{e^{im\theta}}{\sqrt{2\pi}}\left[\frac{1}{\sqrt{N_c}}\sum_j e^{ikjd}\phi(x-jd)\right], \quad \text{(A1)}$$

where $\vec{r}=(x,\vec{\rho})$ is the three-dimensional (3D) position vector, $\vec{\rho}=(y,z)$ is a two-dimensional position vector in the yz plane, θ is the azimuth angle, $m=0,\pm1,\pm2,\ldots$ is the angular quantum number, k is the wave number of electrons in the x direction, $x=jd$ with $j=0,\pm1,\pm2,\ldots$ gives the position for the center of the jth unit cell, d is the superlattice period, and N_c represents the total number of unit cells in the superlattice. In the nearest-neighbor tight-binding model, the corresponding kinetic energy of electrons in the $\Psi_k(\vec{r})$ state is given by $\varepsilon_k=W[1-\cos(kd)]/2$, where $|k|\le\pi/d$ in the first Brillouin zone.

Using the tight-binding wave function given by Eq. (A1), the form factor $\mathcal{F}(q)$ first introduced in Eq. (35) is calculated as

$$\mathcal{F}(q)=\int dx e^{iqx}|\phi(x)|^2=\exp\left(-\frac{q^2\lambda^2}{4}\right), \quad \text{(A2)}$$

where we assume that $|\phi(x)|^2=\exp(-x^2/\lambda^2)/(\lambda\sqrt{\pi})$ with $\lambda\le d/2$ being a half width.

APPENDIX B: INDUCED OPTICAL POLARIZATION

The induced optical polarization of the system first introduced in Eq. (36) can be calculated by means of[47]

$$\mathcal{P}(q)=\frac{ie}{\mathcal{S}d}\int dx\,\delta n(x;\omega)\left(\frac{e^{iqx}}{q}\right)=\frac{2ie}{\mathcal{S}d}\sum_{k,k'}\Pi^{(0)}_{k,k'}(\tilde{\omega})\times\mathcal{H}'_{k,k'}\left[\frac{\mathcal{F}(q)}{q}\right]\delta_{k',k+q+lG}, \quad \text{(B1)}$$

where l is an arbitrary integer, $G=2\pi/d$ and $\mathcal{S}=\pi R^2$ is the sample cross-sectional area. A further detailed calculation of Eq. (B1) yields

$$\mathcal{P}(q)=\frac{-e^2}{\mathcal{S}d}\chi^{(0)}(q;\omega-qv_d)\left[\frac{\mathcal{F}(q)}{q}\right]\sum_{l'}\left[\frac{\mathcal{F}^*(q+l'G)}{(q+l'G)}\right]\times\mathcal{E}_{op}(q+l'G). \quad \text{(B2)}$$

Here, $\chi^{(0)}(q;\tilde{\omega})\equiv\chi^{(0)}(q;\omega-qv_d)$ in Eq. (B2) is the Doppler-shifted irreducible polarization, given by

$$\chi^{(0)}(q;\tilde{\omega}) = 2\sum_k \Pi^{(0)}_{k,k+q}(\tilde{\omega}) = \left(\frac{2Wd}{\pi\hbar^2\tilde{\omega}^2}\right)\sin^2\left(\frac{qd}{2}\right)\left\{\int_{-\pi/d}^{\pi/d} dk f_k \cos(kd) \times \frac{1}{[1-(W/\hbar\tilde{\omega})\sin(qd/2)\sin[(k+q/2)d]+i0^+][1-(W/\hbar\tilde{\omega})\sin(qd/2)\sin[(k-q/2)d]+i0^+]}\right\}$$
$$\approx \left[\int_{-\pi/d}^{\pi/d} dk f_k \cos(kd)\right]\frac{2Wd\,\sin^2(qd/2)}{\pi(\hbar\tilde{\omega}+i0^+)^2}, \tag{B3}$$

where we denote $f_k \equiv f(k,t)$ for a short notation. In q. (B3), we assume a weak electron-tunneling effect [i.e., $(W/\hbar\tilde{\omega})\sin(qd)\sin(kd) \ll 1$], and that only the leading-term contribution with respect to W is retained for the last approximate equation.

The approximation made in arriving at the last step in Eq. (B3) has significantly simplified the calculations in the paper, and the derived analytical solution highlights the physics involved in the optical probing process. In principle, however, this approximation only holds for weak electron tunneling. In order to justify the approximation made in Eq. (B3), we evaluate the following relative error:

$$\frac{\delta\chi^{(0)}}{\chi^{(0)}} = \int_{-\pi/d}^{\pi/d} dk f_k \cos(kd) \times \mathrm{Re}\left[\frac{1}{1-(W/\hbar\tilde{\omega})\sin(qd/2)\sin[(k+q/2)d]+i0^+} \times \frac{1}{1-(W/\hbar\tilde{\omega})\sin(qd/2)\sin[(k-q/2)d]+i0^+} - 1,\right] \tag{B4}$$

which depends on q and $\tilde{\omega}=\omega-qv_d$, as well as on F_{dc} through f_k.

From our numerical calculations (not shown here) we find that when $\hbar\tilde{\omega}$ is large, $(\delta\chi^{(0)}/\chi^{(0)})$ becomes independent of F_{dc}. However, $(\delta\chi^{(0)}/\chi^{(0)})$ changes with F_{dc} as $\hbar\tilde{\omega}$ approaches zero. There exists an unshifted Z-type feature around a finite value of $\hbar\tilde{\omega}_0$, which is enhanced at smaller values of F_{dc}. The maximum relative error $|\delta\chi^{(0)}/\chi^{(0)}|$ nearby $\hbar\tilde{\omega}_0$ reaches 30% at $F_{\mathrm{dc}}=200$ V/cm. In addition, we also find that when $\hbar\tilde{\omega}$ is either large or zero, $(\delta\chi^{(0)}/\chi^{(0)})$ remains the same for all values of qd. The Z-type feature is found to shift to a higher value of $\hbar\tilde{\omega}$ with increasing qd. However, the maximum relative error $|\delta\chi^{(0)}/\chi^{(0)}|$ is always kept at 15%, independent of qd. From these observations, we conclude that the approximation made in Eq. (B3) can be justified at least for $F_{\mathrm{dc}} \geq 200$ V/cm in the NDC regime. For even lower values of F_{dc}, we expect the results presented in this paper to remain qualitatively unchanged.

APPENDIX C: MANY-BODY SCREENING EFFECT

Using the self-consistent-field theory, the interaction Hamiltonian of the system in the absence of an external field is expressed as[47]

$$\mathcal{H}'_{k,k'} = \frac{1}{N_c}\sum_{j,j'} e^{ik'j'd-ikjd}U_H(q;\omega) \times\left[\int dx e^{-iqx}\phi^*(x-jd)\phi(x-j'd)\right], \tag{C1}$$

where

$$U_H(q;\omega) = \int \rho d\rho[-e\Phi_H(q,\rho;\omega)]. \tag{C2}$$

In Eq. (C2), the perturbed Hartree potential $\Phi_H(q,\rho;\omega)$ can be determined by solving the Poisson's equation, from which we obtain

$$[-e\Phi_H(q,\rho;\omega)] = \frac{e^2}{2\epsilon_0\epsilon_{\mathrm{b}}}\int \frac{d^2\vec{\rho}'}{2\pi}\delta n(q,\rho';\omega) \times K_0(|q||\vec{\rho}-\vec{\rho}'|), \tag{C3}$$

where ϵ_{b} is the dielectric constant of the host material and $K_0(x)$ is the modified Bessel function of the second kind. Also, $\delta n(q,\rho';\omega)$ in Eq. (C3) is the Fourier transform of the density fluctuation $\delta n(x,\rho';\omega)$ in Eq. (33) with respect to x. This is given by $\delta n(q,\rho';\omega)=\delta n(q;\omega)[\alpha^2(\rho')/2\pi]$, and yields by using Eq. (34)

$$\delta n(q;\omega) = \frac{1}{d}\chi^{(0)}(q;\omega-qv_d)\mathcal{F}(q)\sum_l \mathcal{F}^*(q+lG) \times U_H(q+lG;\omega). \tag{C4}$$

Finally, substituting Eqs. (C3) and (C4) into Eq. (C2), we arrive at the following self-consistent equation:

$$U_H(q;\omega) = \chi^{(0)}(q;\omega-qv_d)V_c(|q|)\mathcal{F}(q) \times\left[\sum_l \mathcal{F}^*(q+lG)U_H(q+lG;\omega)\right], \tag{C5}$$

where the Coulomb interaction between electrons in a 1D quantum-dot superlattice is given by[57]

$$V_c(|q|) = \left(\frac{e^2}{2\epsilon_0\epsilon_b d}\right)\int \frac{d^2\vec{\rho}}{2\pi}\alpha^2(\rho)\int \frac{d^2\vec{\rho}'}{2\pi}\alpha^2(\rho')K_0(|q||\vec{\rho}-\vec{\rho}'|). \tag{C6}$$

Replacing q with $q+l'G$ and multiplying both sides of Eq. (C5) by $\mathcal{F}^*(q+l'G)$, we eventually obtain the dielectric function of the system after performing a summation over l'

$$\epsilon(q;\omega) = 1 - \chi^{(0)}(q;\omega - qv_d)\sum_l V_c(|q+lG|)|\mathcal{F}(q+lG)|^2. \tag{C7}$$

By using $\epsilon(q;\omega)$ in Eq. (C7), Eq. (38) is renormalized into

$$\alpha_L(q;\omega) = \frac{-e^2}{\pi\epsilon_0 \mathcal{S}d}\mathcal{A}[F_{\rm dc}] \times \left|\sum_l \frac{\mathcal{F}(q+lG)}{(q+lG)}\right|^2 \frac{2W\sin^2(qd/2)}{[\hbar(\omega - qv_d)+i0^+]^2 - \mathcal{D}^2(q)}. \tag{C8}$$

Therefore, the current-driven effect does not only change the magnitude of the optical response, but may also modify the depolarization shift. The energy at which the absorption peak is located is simply given by $\hbar q v_d + \mathcal{D}(q)$, which depends on $F_{\rm dc}$ through v_d and $\mathcal{A}[F_{\rm dc}]$. Moreover, the peak strength also depends on $F_{\rm dc}$ through $\mathcal{A}[F_{\rm dc}]$.

[1] L. Esaki and R. Tsu, IBM J. Res. Dev. **14**, 61 (1970).
[2] F. G. Bass and E. A. Rubinshtein, Fiz. Tverd. Tela (Leningrad) **19**, 1379 (1977); [Sov. Phys. Solid State **19**, 800 (1977)].
[3] R. A. Suris and B. S. Shchamkhalova, Fiz. Tekh. Poluprovodn. (S.-Peterburg) **18**, 1178 (1984); [Sov. Phys. Semicond. **18**, 738 (1984)].
[4] M. Artaki and K. Hess, Superlattices Microstruct. **1**, 489 (1985).
[5] X. L. Lei, N. J. M. Horing, and H. L. Cui, Phys. Rev. Lett. **66**, 3277 (1991).
[6] A. A. Ignatov, E. P. Dodin, and V. I. Shashkin, Mod. Phys. Lett. B **5**, 1087 (1991).
[7] R. R. Gerhardts, Phys. Rev. B **48**, 9178 (1993).
[8] S. K. Lyo, Phys. Rev. B **77**, 195306 (2008).
[9] A. Sibille, J. F. Palmier, H. Wang, and F. Mollot, Phys. Rev. Lett. **64**, 52 (1990).
[10] H. T. Grahn, K. von Klitzing, K. Ploog, and G. H. Döhler, Phys. Rev. B **43**, 12094 (1991).
[11] A. A. Ignatov, K. F. Renk, and E. P. Dodin, Phys. Rev. Lett. **70**, 1996 (1993).
[12] W. Pan, S. K. Lyo, J. L. Reno, J. A. Simmons, D. Li, and S. R. J. Brueck, Appl. Phys. Lett. **92**, 052104 (2008).
[13] N. Sekine and K. Hirakawa, Phys. Rev. Lett. **94**, 057408 (2005).
[14] J. Feldmann, K. Leo, J. Shah, D. A. B. Miller, J. E. Cunningham, T. Meier, G. von Plessen, A. Schulze, P. Thomas, and S. Schmitt-Rink, Phys. Rev. B **46**, 7252 (1992).
[15] T. Dekorsy, P. Leisching, K. Köhler, and H. Kurz, Phys. Rev. B **50**, 8106 (1994).
[16] M. Först, G. Segschneider, T. Dekorsy, H. Kurz, and K. Köhler, Phys. Rev. B **61**, R10563 (2000).
[17] C. Waschke, H. G. Roskos, R. Schwedler, K. Leo, H. Kurz, and K. Kohler, Phys. Rev. Lett. **70**, 3319 (1993).
[18] A. Bonvalet, J. Nagle, V. Berger, A. Migus, J.-L. Martin, and M. Joffre, Phys. Rev. Lett. **76**, 4392 (1996).
[19] P. H. Bolivar, F. Wolter, A. Müller, H. G. Roskos, H. Kurz, and K. Köhler, Phys. Rev. Lett. **78**, 2232 (1997).
[20] M. M. Dignam and A. A. Grinberg, Phys. Rev. B **50**, 4345 (1994).
[21] T. Meier, G. von Plessen, P. Thomas, and S. W. Koch, Phys. Rev. Lett. **73**, 902 (1994).
[22] F. Rossi, T. Meier, P. Thomas, S. W. Koch, P. E. Selbmann, and E. Molinari, Phys. Rev. B **51**, 16943 (1995).
[23] A. Di Carlo, P. Vogl, and W. Potz, Phys. Rev. B **50**, 8358 (1994).
[24] A. Wacker, Phys. Rep. **357**, 1 (2002).
[25] L. L. Bonilla and H. T. Grahn, Rep. Prog. Phys. **68**, 577 (2005).
[26] H.-B. Lin, H. Zhong, N. Karpowicz, Y. Chen, and X.-C. Zhang, Proc. IEEE **95**, 1514 (2007).
[27] A. Sibille, J. F. Palmier, and F. Laruelle, Phys. Rev. Lett. **80**, 4506 (1998).
[28] Y. Zhu, D. H. Huang, and S. Feng, Phys. Rev. B **40**, 3169 (1989).
[29] W.-M. Que and G. Kirczenow, Phys. Rev. B **38**, 3614 (1988).
[30] D. H. Huang and P. R. Antoniewicz, Phys. Rev. B **43**, 2169 (1991).
[31] M. Galperina and A. Nitzan, J. Chem. Phys. **124**, 234709 (2006).
[32] V. V. Pavlovich and E. M. Epshtein, Fiz. Tekh. Poluprovodn. (S.-Peterburg) **10**, 2001 (1976); [Sov. Phys. Semicond. **10**, 1196 (1976)].
[33] A. A. Ignatov, E. Schomburg, J. Grenzer, K. F. Renk, and E. P. Dodin, Z. Phys. B: Condens. Matter **98**, 187 (1995).
[34] X.-G. Zhao, G. A. Georgakis, and Q. Niu, Phys. Rev. B **56**, 3976 (1997).
[35] Duan Suqing, W. Zhang, and X.-G. Zhao, Physica B **299**, 159 (2001).
[36] Z.-G. Wang, Duan Suqing, and X.-G. Zhao, Phys. Rev. B **69**, 035305 (2004).
[37] Duan Suqing, W. Zhang, and X.-G. Zhao, Phys. Rev. B **62**, 9943 (2000).
[38] D. H. Dunlap and V. M. Kenkre, Phys. Rev. B **34**, 3625 (1986).
[39] V. I. Puller, N. J. M. Horing, Lev G. Mourokh, and A. Yu. Smirnov, Phys. Lett. A **281**, 70 (2001).
[40] M. M. Dignam and C. M. de Sterke, Phys. Rev. Lett. **88**, 046806 (2002).
[41] M. J. Zhu, X.-G. Zhao, and Q. Niu, J. Phys.: Condens. Matter **11**, 4527 (1999).
[42] S. K. Lyo and D. H. Huang, Phys. Rev. B **66**, 155307 (2002).
[43] S. K. Lyo and D. H. Huang, Phys. Rev. B **68**, 115317 (2003).
[44] S. K. Lyo and D. H. Huang, Phys. Rev. B **64**, 115320 (2001).
[45] S. E. Koonin and D. C. Meredith, *Computational Physics (Fortran Version)* (Addison-Wesley, Reading, MA, 1990), p. 6.
[46] S. K. Lyo and D. H. Huang, Phys. Rev. B **73**, 205336 (2006).
[47] D. H. Huang, G. Gumbs, V. Fessatidis, and N. J. M. Horing, J.

Phys.: Condens. Matter **6**, 9219 (1994).
[48] D. Grecu, J. Phys. C **8**, 2627 (1975).
[49] D. H. Huang and S. X. Zhou, Phys. Rev. B **38**, 13061 (1988); **38**, 13069 (1988).
[50] X. L. Lei, J. Phys.: Condens. Matter **4**, 9367 (1992).
[51] S. K. Lyo, Phys. Rev. B **40**, 6458 (1989).
[52] P. E. Parris, M. Kuś, and V. M. Kenkre, Phys. Lett. A **289**, 188 (2001).
[53] S. Rott, P. Binder, N. Linder, and G. H. Döhler, Phys. Rev. B **59**, 7334 (1999).
[54] Yu. A. Kosevich, Phys. Rev. B **63**, 205313 (2001).
[55] S. K. Lyo, Phys. Rev. B **64**, 113311 (2001).
[56] S. Winnerl, E. Schomburg, J. Grenzer, H.-J. Regl, A. A. Ignatov, A. D. Semenov, K. F. Renk, D. G. Pavel'ev, Yu. Koschurinov, B. Melzer, V. Ustinov, S. Ivanov, S. Schaposchnikov, and P. S. Kop'ev, Phys. Rev. B **56**, 10303 (1997).
[57] Y. Zhu and S. X. Zhou, J. Phys. C **21**, 3063 (1988).